A new 3D model for Magnetic Particle Imaging using realistic magnetic field topologies for algebraic reconstruction

Gaël Bringout[1,2], **Wolfgang Erb**[3], **Jürgen Frikel**[4]

[1] Universität zu Lübeck, Ratzeburger Allee 160, 23562 Lübeck, Germany
[2] Physikalisch-Technische Bundesanstalt (PTB), Abbestr. 2-12, 10587 Berlin-Charlottenburg, Germany
[3] Università degli Studi di Padova, Via Trieste 63, 35121 Padova, Italy
[4] Ostbayerische Technische Hochschule Regensburg, Galgenbergstr. 32, 93053 Regensburg, Germany

E-mail: gael.bringout@gmail.com, wolfgang.erb@lissajous.it, juergen.frikel@oth-regensburg.de

Abstract. We derive a new 3D model for Magnetic Particle Imaging (MPI) that is able to incorporate realistic magnetic fields in the reconstruction process. In real MPI scanners, the generated magnetic fields have distortions that lead to deformed magnetic low-field volumes (LFV) with the shapes of ellipsoids or bananas instead of ideal field-free points (FFP) or lines (FFL), respectively. Most of the common model-based reconstruction schemes in MPI use however the idealized assumption of an ideal FFP or FFL topology and, thus, generate artifacts in the reconstruction. Our model-based approach is able to deal with these distortions and can generally be applied to dynamic magnetic fields that are approximately parallel to their velocity field. We show how this new 3D model can be discretized and inverted algebraically in order to recover the magnetic particle concentration. To model and describe the magnetic fields, we use decompositions of the fields in spherical harmonics. We complement the description of the new model with several simulations and experiments, exploring the effects of magnetic fields distortion and reconstruction parameters on the reconstruction.

Keywords: Magnetic Particle Imaging (MPI), model-based algebraic reconstruction, description of magnetic fields with spherical harmonics, MPI model for realistic magnetic fields, low-field volume, field-free line, field-free point, reconstruction artifacts, modelling artifacts

1. Introduction

The smart design of magnetic coils for the generation of oscillating magnetic fields is a key challenge in Magnetic Particle Imaging (MPI) [3, 17]. The generated magnetic fields combined with the non-linear magnetization response of the tracer material consisting of superparamagnetic iron oxide nanoparticles (SPIONs) determine the signal acquisition process in MPI and, ultimately, how the distribution of SPIONs can be reconstructed. For this reason an accurate description and analysis of realistic magnetic fields is essential to study modelling and reconstruction in MPI.

Since the first publication in 2005 [7], Magnetic Particle Imaging has undergone major development steps based on a few major designs for the generation of magnetic fields. For two of these topologies, generally referred to as field-free point (FFP)

and field-free line (FFL) topology, fully 3D commercial preclinical MPI scanners are available at the present moment that are able to track SPIONs with a high sensitivity and a high temporal resolution. This makes the biomedical imaging modality MPI to a promising tracer-based diagnostic tool, in particular for blood flow imaging or for quantitative stem cell imaging [20, 24, 26].

In the original scanner design for MPI developed at Philips research (introduced in [7], extended to a full in vivo 3D design in [32]), a static gradient field and a space-homogeneous time-varying drive field are combined in order to magnetize the SPIONs. The two fields are generated in such a way that a moving spot is created, at the center of which the resulting magnetic field is low. The center of this low-field spot in which the magnetic field ideally vanishes is called the field-free point (FFP). As soon as the FFP moves over a distribution of SPIONs, the magnetization of the SPIONs starts to flip, inducing a measurable voltage signal in one or several receive coils. From this time-dependent voltage signal the position of the SPIONs can be reconstructed. In the original design [7, 32], the FFP of the created field moves along a 3D Lissajous trajectory inside a rectangular volume. Later on, other FFP-trajectories have been introduced in MPI, see [16].

In [31], a second major design principle for magnetic fields was introduced in which the applied magnetic fields ideally vanish along a field-free line (FFL). Compared to the FFP setting, the voltage signal is now created in a much larger area along an FFL, providing a higher sensitivity [31] during the scan. A second main advantage of the FFL topology is the availability of an efficient model-based reconstruction formula based on the inverse Radon transform [19].

For both field topologies, FFP and FFL, models for the reconstruction of the particle density have been derived. However, only in very idealized settings, as for a 1D-FFP along line segments [5, 8, 25] or a non-rotating FFL [3, 6, 19], simple and reliable reconstruction formulas are available. While these simple formulas can be incorporated successfully also in 2D and 3D reconstructions [9, 22, 27], they lead to artifacts once the directions of the magnetic fields are altering quickly, as for instance if the FFP is moving on a 3D Lissajous curve. This discrepancy is due to limited possibilities to describe the magnetization behavior of nonuniform anisotropic SPIONs correctly if the external magnetic fields are changing rapidly their orientation. In this case, complex numerical simulations of the Fokker-Planck equations for coupled Brown/Néel rotations are necessary to describe the imaging properly, see [13, 15, 30].

In practice, the signal is not only created on or along an FFP or FFL, but around it, in a low-field volume (LFV). Moreover, real magnetic fields involved in the generation of an FFP or an FFL contain distortions. In particular in the FFL setting, the LFV of the field has more the appearance of a slightly bended banana than that of a straight line [3, 6]. While using the inverse Radon transform for signals created by an ideal FFL yields a reasonable recovery of the particle concentration, this is no longer the case for realistic magnetic fields. In this case, the given distortions lead to artifacts in the reconstruction, in particular at the boundary of the field of view (as illustrated in the Fig. 5 and 6 below). A further problem arises from the particular dynamic generation of the FFL. In order to accelerate the signal acquisition process, the FFL is continuously rotated with a frequency f_{rot} [18]. As the classical filtered back-projection is computed on a rectangular grid in Radon space, the regridding from the rotated Radon information causes additional artifacts in the reconstruction.

The goal of this article is to introduce and study a new 3D model for MPI that is able to incorporate realistic magnetic fields, and to provide a simple reconstruction

algorithm at the same time. More precisely, for realistic uni-directional time-oscillating magnetic fields we aim at obtaining a model-based reconstruction formula that generalizes the known FFL and 1D-FFP formulas in MPI. This new model-based reconstruction reduces artifacts generated by distortions and the rotation dynamics of the magnetic fields and allows us to calculate the particle concentration in an efficient way based on an algebraic reconstruction method.

To this end, we introduce a family of magnetic fields in which the field is parallel to its own velocity field. For this family of fields, the direction of the field does not change over time, allowing to substitute the general MPI imaging equation with a simpler 3D integral equation that can be discretized in an efficient way. In the mathematical formulation we use spherical harmonic expansions of magnetic fields (as introduced in [3, 4, 29]) and, as important examples, we show that this modelling framework includes classical (ideal) models, like the 1D-FFP along a straight line [5, 25] and the ideal FFL [19]. In particular, we show that this formulation offers enough flexibility to model realistic magnetic fields, e.g. in an FFL-type setting, by including higher order harmonics into the expansion. The coefficients of the higher order harmonics can be measured in a calibration procedure providing a realistic MPI model for a particular scanner. In this context, our MPI modelling framework can be interpreted as a hybrid between model-based and measurement-based approach in which the parameters of the magnetic fields are determined in a preliminary step.

1.1. Contributions

(i) We introduce a new modelling framework in MPI based on the expansion of magnetic fields in spherical harmonics and homogeneous harmonic polynomials, and we show how ideal and realistic magnetic field topologies in MPI can be modelled within this framework.

(ii) We state a new 3D MPI model for magnetic fields in which the velocity and the acceleration field are parallel. Applied to ideal cases, this general model explains the standard 1D-FFP and FFL reconstruction formulas.

(iii) We use this new model to obtain a model-based reconstruction that is able to handle realistic magnetic fields in FFL-type imaging. This new model-based approach is able to reduce artifacts in the reconstruction caused by idealized assumptions on the magnetic fields.

(iv) We give a numerical implementation of this reconstruction scheme and provide several simulations and experiments complementing our results.

1.2. Outline of the paper

We continue this introductory part by giving a brief overview about the general imaging concepts in MPI (Section 2). We further give a mathematical description of important ideal and realistic magnetic field topologies encountered in MPI (Section 3). The new model used for the algebraic reconstruction of the particle concentration with realistic field topologies is derived in Section 4. It is formulated in terms of magnetic fields that are parallel to their velocity field. This family of fields contains all relevant ideal and realistic topologies in the considered FFL-type imaging scenario. The numerical details to obtain a discrete system matrix from the given continuous model, including approximation and discretization techniques, are provided in Section 5. Finally, the experiments in Section 6 show that the new algebraic reconstruction

approach based on a model with realistic magnetic fields is very promising and outperforms a direct reconstruction using a filtered back projection. We conclude this article in Section 7. Since our presentation is focused on the FFL-type imaging situation, we show in the appendix how the FFP-type imaging model can be derived within our modelling framework.

2. Principles of MPI signal generation

2.1. General imaging model in MPI

The basic concept of Magnetic Particle Imaging (MPI) is to recover a density $c(\boldsymbol{r})$ of SPIONs from their non-linear magnetization in an applied time-varying magnetic field $\boldsymbol{B}(\boldsymbol{r},t)$. In an MPI scanner, this change in the magnetization of the superparamagnetic particles is measuered in terms of voltage signals induced in one or several receive coils. Neglecting particle-particle interactions, the corresponding general imaging equation is determined by Faraday's law of induction and is given as ([17, Eq. (2.36)])

$$u_\nu(t) = -\mu_0 \frac{\mathrm{d}}{\mathrm{d}t} \int_\Omega \left\langle \boldsymbol{\varrho}_\nu(\boldsymbol{r}), \overline{\boldsymbol{M}}(\boldsymbol{B}(\boldsymbol{r},t)) \right\rangle \, c(\boldsymbol{r}) \, \mathrm{d}\boldsymbol{r}. \tag{1}$$

In this formula, the signal $u_\nu : \mathbb{R} \to \mathbb{R}$ denotes the induced voltage $u_\nu(t)$ for a given receive coil $\nu \in \{1, \dots, V\}$ at a time t, and the constant μ_0 the permeability in free space. The function $\boldsymbol{\varrho}_\nu : \Omega \to \mathbb{R}^3$ on the domain $\Omega \subset \mathbb{R}^3$ describes the sensitivity vector of the receive coil ν pointing in direction of the central axis of the coil. The function $c : \Omega \to \mathbb{R}_+$ describes the density $c(\boldsymbol{r})$ of the magnetic particles at a point $\boldsymbol{r} \in \Omega$. Finally, $\overline{\boldsymbol{M}} : \mathbb{R}^3 \to \mathbb{R}^3$ gives the magnetization response of a single mean SPION depending on the applied magnetic field $\boldsymbol{B}(\boldsymbol{r},t)$ at position $\boldsymbol{r}$ and time t.

This equation describes a general imaging situation in MPI. For a particular measurement setup the sensitivities $\boldsymbol{\varrho}_\nu$, the magnetization response function $\overline{\boldsymbol{M}}$ and the employed magnetic fields $\boldsymbol{B}(\boldsymbol{r},t)$ have to be modelled or specified.

2.2. Magnetic fields and magnetization

The magnetization $\overline{\boldsymbol{M}}$ of a single SPION is aligned along the direction of the applied magnetic field $\boldsymbol{B}(\boldsymbol{r},t)$ and can be written as

$$\overline{\boldsymbol{M}}(\boldsymbol{B}(\boldsymbol{r},t)) = \bar{\mathrm{m}}(|\boldsymbol{B}(\boldsymbol{r},t)|) \, \frac{\boldsymbol{B}(\boldsymbol{r},t)}{|\boldsymbol{B}(\boldsymbol{r},t)|}. \tag{2}$$

A classical way to describe the modulus $\bar{\mathrm{m}}$ of the magnetization is the Langevin theory of paramagnetism. In this theory the mean modulus $\bar{\mathrm{m}}$ is modelled as

$$\bar{\mathrm{m}}(|\boldsymbol{B}|) = m_0 L(\lambda |\boldsymbol{B}|), \tag{3}$$

with the Langevin function $L : \mathbb{R} \to \mathbb{R}$ and the constant λ given by

$$L(x) = \coth x - \frac{1}{x} \quad \text{and} \quad \lambda = \frac{\mu_0 m_0}{k_\mathrm{B} T}.$$

Here, m_0 denotes the magnetic moment of a single SPION, μ_0 again the permeability in free space, k_B the Boltzmann constant, and T the temperature. The Langevin

function $L(x)$ is an odd function satisfying $\lim_{x\to\pm\infty} L(x) = \pm 1$. Its derivative is given by

$$L'(x) = \begin{cases} \frac{1}{3}, & x = 0, \\ \frac{1}{x^2} - \frac{1}{\sinh^2(x)}, & x \neq 0. \end{cases} \tag{4}$$

For the modulus $\bar{\mathrm{m}}$, we therefore get $\bar{\mathrm{m}}'(|\boldsymbol{B}|) = m_0 \lambda L'(\lambda|\boldsymbol{B}|)$ and asymptotically $\lim_{|\boldsymbol{B}|\to\infty} \bar{\mathrm{m}}(|\boldsymbol{B}|) = m_0$. For a large vector field strength $|\boldsymbol{B}|$ the saturation of the magnetization is therefore described by m_0. The derivative $\bar{\mathrm{m}}'(0) = m_0\lambda/3$ is a measure for the magnetic susceptibility of a particle.

2.3. Extension of curl- and divergence-free magnetic fields

In a volume with no magnetic field source and constant permeability μ_0, as for instance in the interior of a cylindrical coil, a magnetic field $\boldsymbol{B}$ can be regarded both as a divergence-free and a curl-free vector field (see [3, Section 2.1.2] or [11, Section 5.4]), i.e. it satisfies the two equations

$$\nabla \cdot \boldsymbol{B} = 0 \quad \text{and} \quad \nabla \times \boldsymbol{B} = \boldsymbol{0}.$$

The second identity implies that $\boldsymbol{B}$ is locally a conservative vector field and can be written as the gradient $\boldsymbol{B} = \nabla\varphi_{\boldsymbol{B}}$ of a potential function $\varphi_{\boldsymbol{B}}$. The fact that $\boldsymbol{B}$ is divergence-free then implies that $\varphi_{\boldsymbol{B}}$ satisfies the Laplace equation $\Delta\varphi_{\boldsymbol{B}} = 0$. In particular, assuming that the vector field $\boldsymbol{B}$ is sufficiently smooth, the identity $\Delta\varphi_{\boldsymbol{B}} = 0$ implies that also every component B_j of the vector field $\boldsymbol{B} = (B_1, B_2, B_3)$ is a solution of the Laplace equation $\Delta B_j = 0$, $j \in \{1, 2, 3\}$. As proposed in [4], this fact enables us to extend the components B_j of the vector field $\boldsymbol{B}$ in terms of spherical harmonics in order to get a compact description of the magnetic fields in MPI.

2.3.1. Homogeneous harmonic polynomials. A homogeneous polynomial in $\mathbb{R}^3$ of degree $l \in \mathbb{N}_0$ is a linear combination of the monomials

$$x^{i_1} y^{i_2} z^{i_3}, \quad i_1 + i_2 + i_3 = l.$$

The space $\mathcal{P}_l$ of all homogeneous polynomials of degree l has the dimension

$$\dim \mathcal{P}_l = \frac{(l+1)(l+2)}{2}.$$

Herein, the subspace $\mathcal{H}_l$ of homogeneous harmonic polynomials of degree l is given by the polynomials $p \in \mathcal{P}_l$ satisfying the Laplace equation

$$\Delta p(x, y, z) = 0.$$

In this way, the spaces $\mathcal{H}_l$ are natural candidates to approximate and expand the components B_i of the magnetic field $\boldsymbol{B}$. The dimension of the harmonic spaces $\mathcal{H}_l$ is given by $\dim \mathcal{H}_l = \dim \mathcal{P}_l - \dim \mathcal{P}_{l-2} = 2l + 1$.

2.3.2. Spherical harmonics. A homogeneous harmonic polynomial $p \in \mathcal{H}_l$ of degree $l \in \mathbb{N}_0$ can be written in spherical coordinates (r, θ, φ) as a linear combination of

Table 1: Spherical harmonics and harmonic homogeneous polynomials of degree $l \leq 2$.

Degree l	$Y_{l,m}(\theta,\varphi)$	$p_{l,m}(\boldsymbol{r})$
0	$Y_{0,0}(\theta,\varphi) = 1$	$p_{0,0}(\boldsymbol{r}) = 1$
1	$Y_{1,1}(\theta,\varphi) = \sin\theta\cos\varphi$	$p_{1,1}(\boldsymbol{r}) = x$
	$Y_{1,0}(\theta,\varphi) = \cos\theta$	$p_{1,0}(\boldsymbol{r}) = z$
	$Y_{1,-1}(\theta,\varphi) = \sin\theta\sin\varphi$	$p_{1,-1}(\boldsymbol{r}) = y$
2	$Y_{2,2}(\theta,\varphi) = \frac{\sqrt{3}}{2}\sin^2\theta\cos 2\varphi$	$p_{2,2}(\boldsymbol{r}) = \frac{\sqrt{3}}{2}(x^2-y^2)$
	$Y_{2,1}(\theta,\varphi) = \sqrt{3}\sin\theta\cos\theta\cos\varphi$	$p_{2,1}(\boldsymbol{r}) = \sqrt{3}xz$
	$Y_{2,0}(\theta,\varphi) = \frac{1}{2}(3\cos^2\theta - 1)$	$p_{2,0}(\boldsymbol{r}) = z^2 - \frac{1}{2}x^2 - \frac{1}{2}y^2$
	$Y_{2,-1}(\theta,\varphi) = \sqrt{3}\sin\theta\cos\theta\sin\varphi$	$p_{2,-1}(\boldsymbol{r}) = \sqrt{3}yz$
	$Y_{2,-2}(\theta,\varphi) = \frac{\sqrt{3}}{2}\sin^2\theta\sin 2\varphi$	$p_{2,-2}(\boldsymbol{r}) = \sqrt{3}xy$

particular basis functions defined in terms of spherical harmonics. Namely, with the spherical coordinates given by

$$(x,y,z) = (r\sin\theta\cos\varphi, r\sin\theta\sin\varphi, r\cos\theta),$$

the polynomials

$$p_{l,m}(r,\theta,\varphi) = r^l Y_{l,m}(\theta,\varphi), \quad m = -l,\dots,l,$$

form a basis for the space $\mathcal{H}_l$ of harmonic polynomials. Here, $Y_{l,m}(\theta,\varphi)$ denote the $2l+1$ real-valued Schmidt semi-normalized spherical harmonics of degree l given by

$$Y_{l,m}(\theta,\varphi) = \begin{cases} \sqrt{2\frac{(l-m)!}{(l+m)!}}P_l^m(\cos\theta)\cos(m\varphi) & \text{if } m \in \{1,\dots,l\}, \\ P_l^0(\cos\theta) & \text{if } m = 0, \\ \sqrt{2\frac{(l-m)!}{(l+m)!}}P_l^{|m|}(\cos\theta)\sin(|m|\varphi) & \text{if } m \in \{-1,-2,\dots,-l\}, \end{cases}$$

where P_l^m, $l, m \in \mathbb{N}$, $0 \leq m \leq l$, denote the associated Legendre polynomials given by

$$P_l^m(x) = \frac{1}{2^l l!}(1-x^2)^{m/2}\,\frac{\mathrm{d}^{l+m}}{\mathrm{d}x^{l+m}}(x^2-1)^l.$$

Note that we omit the frequently used Condon-Shortly phase $(-1)^m$ in the definition of P_l^m (see [11, Section 3.5]). The spherical harmonics and the corresponding harmonic polynomials up to degree $l = 2$ are listed in Table 1.

2.3.3. Expansion of the components B_j in spherical harmonics. If the components B_j of the magnetic field $\boldsymbol{B} = (B_1, B_2, B_3)$ satisfy the Laplace equation, we can expand them in terms of homogeneous harmonic polynomials and obtain the decomposition

$$B_j(x,y,z) = \sum_{l=0}^{\infty}\sum_{m=-l}^{l} c_{l,m}^j p_{l,m}(x,y,z), \quad j \in \{1,2,3\},$$

or, in spherical coordinates,

$$B_j(r,\theta,\varphi) = \sum_{l=0}^{\infty}\sum_{m=-l}^{l} c_{l,m}^j r^l Y_{l,m}(\theta,\varphi), \quad j \in \{1,2,3\}.$$

Table 2: Spherical harmonic coefficients of a 2D rotating FFL using ideal magnetic fields

Coil name	B_1	B_2	B_3	Time dependent part
Select Maxwell	$c_{11}^1 = -g$	$c_{1-1}^2 = -g$	$c_{10}^3 = 2g$	1
Select Quad 0	$c_{11}^1 = g$	$c_{1-1}^2 = -g$		$\cos 2\pi f_{\mathrm{rot}} t$
Select Quad 45	$c_{1-1}^1 = g$	$c_{11}^2 = g$		$\sin 2\pi f_{\mathrm{rot}} t$
x-drive	$c_{00}^1 = d$			$\sin 2\pi f_{\mathrm{d}} t \ \sin \pi f_{\mathrm{rot}} t$
y-drive		$c_{00}^2 = d$		$-\sin 2\pi f_{\mathrm{d}} t \ \cos \pi f_{\mathrm{rot}} t$

We assume that the magnetic fields are properly smooth, so that there are no issues with convergence at this place.

3. Ideal and realistic magnetic fields in MPI

All major magnetic field topologies in MPI can be written compactly in terms of spherical harmonic expansions for a few involved generating fields. In the following, we review the (ideal) magnetic field topology generating a field-free line (FFL) and provide the mathematical representation with respect to the spherical harmonics expansion. We also explain how such expansions can be obtained for realistic magnetic field topologies. Further interesting descriptions of classical field topologies generating a field-free point along a Lissajous curve and a line segment are given in Section 8.1 and Section 8.2 of the appendix.

3.1. Ideal rotating field-free line (FFL) in the xy-plane

A magnetic field topology to generate a dynamically rotating field-free line (FFL) in the xy-plane was developed in [6]. The building elements of this rotating FFL are listed in Table 2, see also [3] for a derivation.

The complete magnetic field $\boldsymbol{B}(\boldsymbol{r}, t)$ to generate the rotating FFL is given by

$$\begin{aligned}
\boldsymbol{B}(\boldsymbol{r}, t) &= \boldsymbol{B}_{\mathrm{Maxwell}}(\boldsymbol{r}) + \boldsymbol{B}_{\mathrm{Quad0}}(\boldsymbol{r}) \cos(2\pi f_{\mathrm{rot}} t) + \boldsymbol{B}_{\mathrm{Quad45}}(\boldsymbol{r}) \sin(2\pi f_{\mathrm{rot}} t) \\
&\quad + \boldsymbol{B}_{\mathrm{x-drive}}(\boldsymbol{r}) \sin(2\pi f_{\mathrm{d}} t) \sin(\pi f_{\mathrm{rot}} t) - \boldsymbol{B}_{\mathrm{y-drive}}(\boldsymbol{r}) \sin(2\pi f_{\mathrm{d}} t) \cos(\pi f_{\mathrm{rot}} t) \\
&= g \begin{pmatrix} -x \\ -y \\ 2z \end{pmatrix} + g \begin{pmatrix} x \\ -y \\ 0 \end{pmatrix} \cos(2\pi f_{\mathrm{rot}} t) + g \begin{pmatrix} y \\ x \\ 0 \end{pmatrix} \sin(2\pi f_{\mathrm{rot}} t) \\
&\quad + \begin{pmatrix} d \sin(2\pi f_{\mathrm{d}} t) \sin(\pi f_{\mathrm{rot}} t) \\ -d \sin(2\pi f_{\mathrm{d}} t) \cos(\pi f_{\mathrm{rot}} t) \\ 0 \end{pmatrix}, \qquad (5)
\end{aligned}$$

where f_{d} and f_{rot} denote the drive and rotation frequencies of the FFL. The potential function $\varphi_{\boldsymbol{B}}$ of the conservative vector field $\boldsymbol{B}(\boldsymbol{r}, t)$ has the form

$$\varphi_{\boldsymbol{B}}(\boldsymbol{r}, t) = g\Big(z^2 - \big(x \sin(\pi f_{\mathrm{rot}} t) - y \cos(\pi f_{\mathrm{rot}} t)\big)^2\Big) + d\big(x \sin(\pi f_{\mathrm{rot}} t) - y \cos(\pi f_{\mathrm{rot}} t)\big) \sin(2\pi f_{\mathrm{d}} t).$$

We denote by $\mathrm{FFL}(t)$ the set of all $\boldsymbol{r}$ at which the field $\boldsymbol{B}(\boldsymbol{r}, t)$ vanishes at $t \in \mathbb{R}$.

Lemma 3.1. *The field-free line* $\mathrm{FFL}(t)$ *at a time* $t \in \mathbb{R}$ *can be parametrized as*

$$\begin{aligned}\mathrm{FFL}(t) &= \left\{ \begin{pmatrix} \cos(\pi f_{\mathrm{rot}} t) \\ \sin(\pi f_{\mathrm{rot}} t) \\ 0 \end{pmatrix} h + \frac{d}{2g} \begin{pmatrix} \sin(\pi f_{\mathrm{rot}} t)\sin(2\pi f_{\mathrm{d}} t) \\ -\cos(\pi f_{\mathrm{rot}} t)\sin(2\pi f_{\mathrm{d}} t) \\ 0 \end{pmatrix} \;\middle|\; h \in \mathbb{R} \right\} \\ &= \left\{ (x, y, 0) : \; \sin(\pi f_{\mathrm{rot}} t)x - \cos(\pi f_{\mathrm{rot}} t)y = \frac{d}{2g}\sin(2\pi f_{\mathrm{d}} t) \right\}.\end{aligned}$$

The set $\mathrm{FFL}(t)$ *is a line in the xy-plane perpendicular to* $(\sin(\pi f_{\mathrm{rot}} t), -\cos(\pi f_{\mathrm{rot}} t), 0)$ *and with distance* $|\frac{d}{2g}\sin(2\pi f_{\mathrm{d}} t)|$ *to the origin.*

Proof. Every point $\boldsymbol{r} = (x, y, z)$ in the set $\mathrm{FFL}(t)$ satisfies by definition $\boldsymbol{B}(\boldsymbol{r}, t) = \boldsymbol{0}$. Therefore, the formula (5) for $\boldsymbol{B}(\boldsymbol{r}, t)$ gives $z = 0$, and for x and y the system of equations

$$g \begin{pmatrix} x(1 - \cos(2\pi f_{\mathrm{rot}} t)) \\ y(1 + \cos(2\pi f_{\mathrm{rot}} t)) \end{pmatrix} - g \begin{pmatrix} y \\ x \end{pmatrix} \sin(2\pi f_{\mathrm{rot}} t) = \begin{pmatrix} d\sin(2\pi f_{\mathrm{d}} t)\sin(\pi f_{\mathrm{rot}} t) \\ -d\sin(2\pi f_{\mathrm{d}} t)\cos(\pi f_{\mathrm{rot}} t) \end{pmatrix}.$$

Factoring out the term $\sin(\pi f_{\mathrm{rot}} t)$ in the first line and $\cos(\pi f_{\mathrm{rot}} t)$ in the second, we can simplify this expression as

$$\left(\sin(\pi f_{\mathrm{rot}} t)x - \cos(\pi f_{\mathrm{rot}} t)y - \frac{d}{2g}\sin(2\pi f_{\mathrm{d}} t) \right) \begin{pmatrix} \sin(\pi f_{\mathrm{rot}} t) \\ \cos(\pi f_{\mathrm{rot}} t) \end{pmatrix} = \boldsymbol{0}. \tag{6}$$

Identity (6) implies that $\sin(\pi f_{\mathrm{rot}} t)x - \cos(\pi f_{\mathrm{rot}} t)y - \frac{d}{2g}\sin(2\pi f_{\mathrm{d}} t) = 0$ and, thus, the second stated characterization of the FFL. In particular, it implies that all admissible points (x, y) lie on a line in the xy-plane perpendicular to $(\sin(\pi f_{\mathrm{rot}} t), -\cos(\pi f_{\mathrm{rot}} t), 0)$. From this normal form of the FFL the parametrized description of the FFL given in Lemma 3.1 follows with a standard linear algebra argument. □

3.2. Non-rotating FFL in the xy plane

We can slightly modify the magnetic fields from the last subsection to generate non-rotating FFL's. For this, it is only necessary to substitute the time-depending rotating angle $2\pi f_{\mathrm{rot}} t$ in (5) with a fixed angle $\alpha \in [0, 2\pi]$. The corresponding magnetic field for a non-rotating FFL is given by

$$\boldsymbol{B}(\boldsymbol{r}, t) = 2g \begin{pmatrix} (y\cos\frac{\alpha}{2} - x\sin\frac{\alpha}{2})\sin\frac{\alpha}{2} \\ (x\sin\frac{\alpha}{2} - y\cos\frac{\alpha}{2})\cos\frac{\alpha}{2} \\ z \end{pmatrix} + \begin{pmatrix} d\sin(2\pi f_{\mathrm{d}} t)\sin\frac{\alpha}{2} \\ -d\sin(2\pi f_{\mathrm{d}} t)\cos\frac{\alpha}{2} \\ 0 \end{pmatrix}.$$

From Lemma 3.1 we can derive that $\mathrm{FFL}(t)$ is in this case given as

$$\mathrm{FFL}(t) = \left\{ \boldsymbol{r} \mid \langle \boldsymbol{e}_\alpha, \boldsymbol{r} \rangle = \frac{d}{2g}\sin(2\pi f_{\mathrm{d}} t) \right\},$$

where $\boldsymbol{e}_\alpha = (\sin\left(\frac{\alpha}{2}\right), -\cos\left(\frac{\alpha}{2}\right), 0)$ denotes the normal vector of the FFL in the xy-plane. In particular, the direction of the FFL is now independent of the time t.

3.3. Realistic magnetic fields in Magnetic Particle Imaging

While the ideal field topologies of the last sections are represented by only a few spherical harmonics, a realistic magnetic field is accurately described by a larger amount of spherical harmonic coefficients. By incorporating these higher order spherical harmonics in the description of the magnetic fields a realistic and scanner-adapted model of the magnetic field topologies is obtained. The magnetic field coefficients in the expansion can be determined by measuring the field at a discrete set of spherical nodes with a subsequent numerical evaluation of the spherical integrals providing the inner product between field and spherical harmonics, see [3, 29]. In a second step, the expansion coefficients can then be incorporated into the MPI model that will be introduced in the next section. This calibration procedure is much less time consuming than the one used in an entirely measurement-based approach for MPI, in which a complete system matrix has to be measured [10].

Indeed, comparing the numbers of positions at which a measurement has to be conducted, we can get a rough estimate of the involved time expenses. To acquire the magnetic field representation for the presented method using five different coils and 45 evaluations points per coil based on the Gauss-Legendre quadrature on the sphere [33] (which is exact for all spherical harmonics up to degree $l \leq 4$, see [29] for concrete applications in MPI), we require in total 225 magnetic field measurements to set up our 3D model. Note that this number is independent from the future resolution of the reconstruction. On the other hand, a simple measurement-based approach for the system matrix with a resolution of 2 mm for a circular surface with a diameter of 173 mm would required around 5500 measurements.

Our approach can consequently be considered as a hybrid reconstruction method in which a part of the model (in our case the generating magnetic fields) is measured, but the tracer response is modelled. An example of expansion coefficients for a realistic coil taken from [3] is shown in Fig. 1. While we have seen in Section 3.1 that an ideal y-drive field in the generation of a rotating FFL is represented by a single spherical harmonic coefficient, a corresponding realistic y-drive field contains a large number of higher degree spherical harmonic coefficients. These higher degree spherical harmonics have in return an impact on the LFV of the generated magnetic field. While the ideal magnetic field generates a straight LFV (see Fig. 3b) a corresponding realistic LFV has more the curved shape of a banana (Fig. 3c).

In this work, the spherical harmonic coefficients $c^j_{l,m}$ are obtained via a simulation using a 3D model of the wires used to build the coils of an actual scanner. This model includes most of the imperfection leading to those higher harmonics, like some geometrical variation introduced for the fabrication of the coils or the current path required to connect the different current carrying path of the coil. The details are given in [3].

4. A new 3D MPI model for realistic magnetic fields

In this main section, we derive a new model for MPI that incorporates realistic field topologies and allows for a simple reconstruction at the same time. This model is based on the assumption that the applied magnetic field is parallel to its velocity field. This assumption is general enough to guarantee that realistic FFL-type field topologies are included. Further, we will show that the reconstruction formula for an ideal FFL topology is a special cases of this model.

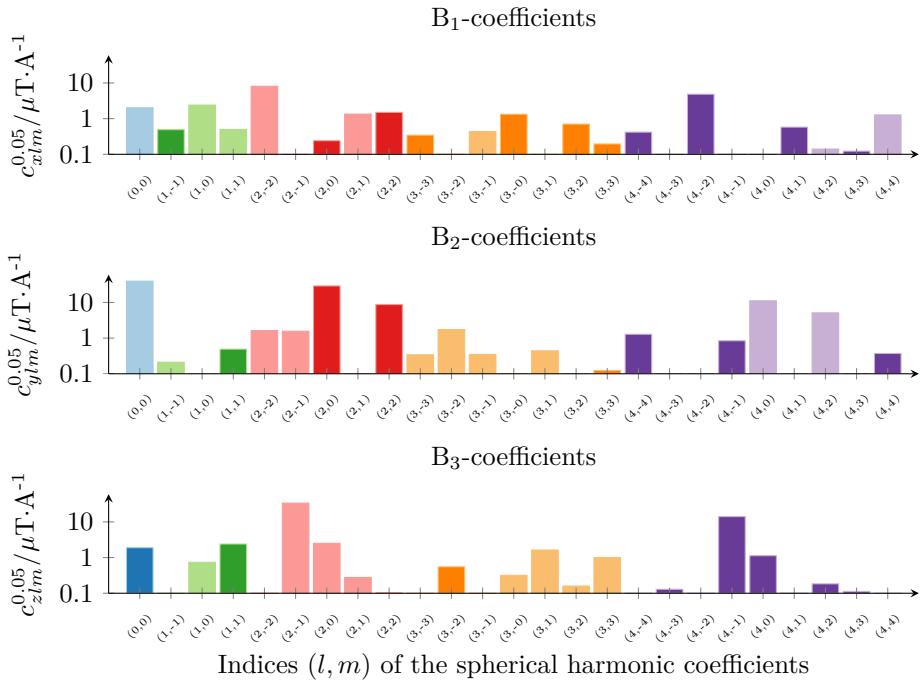

Figure 1: Spherical harmonic coefficients of an MPI y-drive coil from a simulation of a realistic coil. The moduli of the spherical harmonic coefficients $c^j_{l,m}$ are displayed up to degree $l = 4$ and $-4 \leq m \leq 4$ in a sphere with radius $R = 0.05$ m. Light and dark filling colors indicate positive or negative coefficients, respectively.

4.1. An imaging model for magnetic fields with parallel velocity field

A time-dependent magnetic field $\boldsymbol{B}(\boldsymbol{r}, t)$ is called *parallel to its velocity field* if

$$\frac{\mathrm{d}}{\mathrm{d}t}\boldsymbol{B}(\boldsymbol{r}, t) = \lambda(\boldsymbol{r}, t) \cdot \boldsymbol{B}(\boldsymbol{r}, t) \tag{7}$$

holds for some real-valued $\lambda = \lambda(\boldsymbol{r}, t)$ for all $\boldsymbol{r} \in \Omega$, $t \in \mathbb{R}$, as soon as $\boldsymbol{B}(\boldsymbol{r}, t) \neq 0$. In other words, at any position $\boldsymbol{r} \in \Omega$ and time t the direction of the velocity $\frac{\mathrm{d}}{\mathrm{d}t}\boldsymbol{B}(\boldsymbol{r}, t)$ is pointing in the same or in the reversed direction of the magnetic field $\boldsymbol{B}(\boldsymbol{r}, t)$. If $\boldsymbol{B}(\boldsymbol{r}, t) \neq \boldsymbol{0}$ the parallelity (7) implies that the magnetic field $\boldsymbol{B}(\boldsymbol{r}, t)$ does not change it's direction over time:

$$\frac{\mathrm{d}}{\mathrm{d}t}\frac{\boldsymbol{B}(\boldsymbol{r}, t)}{|\boldsymbol{B}(\boldsymbol{r}, t)|} = \frac{1}{|\boldsymbol{B}(\boldsymbol{r}, t)|}\left(\frac{\mathrm{d}}{\mathrm{d}t}\boldsymbol{B}(\boldsymbol{r}, t) - \frac{\boldsymbol{B}(\boldsymbol{r}, t)}{|\boldsymbol{B}(\boldsymbol{r}, t)|}\left\langle \frac{\mathrm{d}}{\mathrm{d}t}\boldsymbol{B}(\boldsymbol{r}, t), \frac{\boldsymbol{B}(\boldsymbol{r}, t)}{|\boldsymbol{B}(\boldsymbol{r}, t)|}\right\rangle\right) = \boldsymbol{0}.$$

In particular, in case of parallelity the acceleration of the magnetic field is also only performed tangentially in direction of the field $\boldsymbol{B}(\boldsymbol{r}, t)$. Namely, we have

$$\frac{\mathrm{d}^2}{\mathrm{d}t^2}\boldsymbol{B}(\boldsymbol{r}, t) = \frac{\boldsymbol{B}(\boldsymbol{r}, t)}{|\boldsymbol{B}(\boldsymbol{r}, t)|}\,\frac{\mathrm{d}^2}{\mathrm{d}t^2}|\boldsymbol{B}(\boldsymbol{r}, t)|.$$

Theorem 4.1. *We assume that the function* $\bar{\mathrm{m}} : \mathbb{R} \to \mathbb{R}$ *is odd and twice continuously differentiable and that the magnetic field* $\boldsymbol{B}(\boldsymbol{r}, t)$ *is differentiable and parallel to its*

velocity field. Then the time derivative of the magnetization $\overline{\boldsymbol{M}}(\boldsymbol{B}(\boldsymbol{r},t))$ *defined in* (2) *can be simplified to*

$$\frac{\mathrm{d}}{\mathrm{d}t}\overline{\boldsymbol{M}}(\boldsymbol{B}(\boldsymbol{r},t)) = \bar{\mathrm{m}}'(|\boldsymbol{B}(\boldsymbol{r},t)|)\,\frac{\mathrm{d}}{\mathrm{d}t}\boldsymbol{B}(\boldsymbol{r},t). \tag{8}$$

In particular, the general MPI imaging model stated in (1) *can be rewritten as*

$$u_\nu(t) = -\mu_0 \int_{\mathbb{R}^3} \left\langle \boldsymbol{\varrho}_\nu(\boldsymbol{r}), \frac{\mathrm{d}}{\mathrm{d}t}\boldsymbol{B}(\boldsymbol{r},t)\right\rangle \bar{\mathrm{m}}'(|\boldsymbol{B}(\boldsymbol{r},t)|)\, c(\boldsymbol{r})\,\mathrm{d}\boldsymbol{r}. \tag{9}$$

Proof. In the case that $\boldsymbol{B}(\boldsymbol{r},t) \neq \boldsymbol{0}$, we use the chain rule to calculate the derivative of the vector field $\overline{\boldsymbol{M}}(\boldsymbol{B}(\boldsymbol{r},t))$ given in (2):

$$\frac{\mathrm{d}}{\mathrm{d}t}\overline{\boldsymbol{M}}(\boldsymbol{B}(\boldsymbol{r},t)) = \bar{\mathrm{m}}'(|\boldsymbol{B}(\boldsymbol{r},t)|)\left\langle \frac{\mathrm{d}}{\mathrm{d}t}\boldsymbol{B}(\boldsymbol{r},t), \frac{\boldsymbol{B}(\boldsymbol{r},t)}{|\boldsymbol{B}(\boldsymbol{r},t)|}\right\rangle \frac{\boldsymbol{B}(\boldsymbol{r},t)}{|\boldsymbol{B}(\boldsymbol{r},t)|} + \bar{\mathrm{m}}(|\boldsymbol{B}(\boldsymbol{r},t)|)\frac{\mathrm{d}}{\mathrm{d}t}\frac{\boldsymbol{B}(\boldsymbol{r},t)}{|\boldsymbol{B}(\boldsymbol{r},t)|}.$$

Since $\boldsymbol{B}(\boldsymbol{r},t)$ is parallel to its velocity field $\frac{\mathrm{d}}{\mathrm{d}t}\boldsymbol{B}(\boldsymbol{r},t)$, we have $\frac{\mathrm{d}}{\mathrm{d}t}\frac{\boldsymbol{B}(\boldsymbol{r},t)}{|\boldsymbol{B}(\boldsymbol{r},t)|} = \boldsymbol{0}$ and $\left\langle \frac{\mathrm{d}}{\mathrm{d}t}\boldsymbol{B}(\boldsymbol{r},t), \frac{\boldsymbol{B}(\boldsymbol{r},t)}{|\boldsymbol{B}(\boldsymbol{r},t)|}\right\rangle \frac{\boldsymbol{B}(\boldsymbol{r},t)}{|\boldsymbol{B}(\boldsymbol{r},t)|} = \frac{\mathrm{d}}{\mathrm{d}t}\boldsymbol{B}(\boldsymbol{r},t)$, and consequently

$$\frac{\mathrm{d}}{\mathrm{d}t}\overline{\boldsymbol{M}}(\boldsymbol{B}(\boldsymbol{r},t)) = \bar{\mathrm{m}}'(|\boldsymbol{B}(\boldsymbol{r},t)|)\,\frac{\mathrm{d}}{\mathrm{d}t}\boldsymbol{B}(\boldsymbol{r},t).$$

In the case that $\boldsymbol{B}(\boldsymbol{r},t) = \boldsymbol{0}$, we take a closer look to the univariate function $\bar{\mathrm{m}}(x)/x$. Since $\bar{\mathrm{m}}$ is odd and twice differentiable, we have

$$\frac{\bar{\mathrm{m}}(x)}{x} \underset{x\to 0}{\longrightarrow} \bar{\mathrm{m}}'(0) \quad \text{and} \quad \frac{\mathrm{d}}{\mathrm{d}x}\frac{\bar{\mathrm{m}}(x)}{x} = \frac{\bar{\mathrm{m}}'(x)x - \bar{\mathrm{m}}(x)}{x^2} \underset{x\to 0}{\longrightarrow} \bar{\mathrm{m}}''(0) = 0,$$

and, thus, that the derivative of the function $\bar{\mathrm{m}}(x)/x$ vanishes at $x = 0$. Therefore, we get also in the case $\boldsymbol{B}(\boldsymbol{r},t) = \boldsymbol{0}$:

$$\frac{\mathrm{d}}{\mathrm{d}t}\overline{\boldsymbol{M}}(\boldsymbol{B}(\boldsymbol{r},t)) = \frac{\mathrm{d}}{\mathrm{d}t}\left(\frac{\bar{\mathrm{m}}(|\boldsymbol{B}(\boldsymbol{r},t)|)}{|\boldsymbol{B}(\boldsymbol{r},t)|}\boldsymbol{B}(\boldsymbol{r},t)\right) = \bar{\mathrm{m}}'(0)\frac{\mathrm{d}}{\mathrm{d}t}\boldsymbol{B}(\boldsymbol{r},t).$$

□

4.2. The 2D-MPI imaging equation for an ideal FFL

As an important example, we show that the reconstruction formula for 2D-MPI imaging with an ideal FFL is a special case of Theorem 4.1. In Subsection 8.3 of the appendix, we will see that Theorem 4.1 implies also the well-known reconstruction formula for 1D-FFP imaging.

In Section 3.2, the magnetic field

$$\boldsymbol{B}(\boldsymbol{r},t) = 2g\begin{pmatrix} -\left(\langle \boldsymbol{e}_\alpha, \boldsymbol{r}\rangle - \frac{d}{2g}\sin(2\pi f_\mathrm{d} t)\right)\sin\frac{\alpha}{2} \\ \left(\langle \boldsymbol{e}_\alpha, \boldsymbol{r}\rangle - \frac{d}{2g}\sin(2\pi f_\mathrm{d} t)\right)\cos\frac{\alpha}{2} \\ z \end{pmatrix}$$

was used to generate the non-rotating $\mathrm{FFL}(t) = \{\boldsymbol{r} \mid \langle \boldsymbol{e}_\alpha, \boldsymbol{r}\rangle = \frac{d}{2g}\sin(2\pi f_\mathrm{d} t)\}$. Here, $\boldsymbol{e}_\alpha = \left(\sin\left(\frac{\alpha}{2}\right), -\cos\left(\frac{\alpha}{2}\right), 0\right)$ denotes the normal vector of the FFL in the xy-plane. The particular definition of $\boldsymbol{B}(\boldsymbol{r},t)$ implies that for all points $\boldsymbol{r}$ in the xy-plane the

magnetic field $\boldsymbol{B}(\boldsymbol{r},t)$ is parallel to its velocity field $\frac{\mathrm{d}}{\mathrm{d}t}\boldsymbol{B}(\boldsymbol{r},t)$. Thus, if we assume that the support $\operatorname{supp} c = \Omega \subset \mathbb{R}^3$ is a compact 2D region in the xy plane, we can use the simplified imaging equation (9) for a model-based reconstruction. Inserting the magnetic field of the non-rotating FFL in the model equation (9) and using a simplified 2D integral over the domain Ω in the xy-plane, we get the formula

$$u_\nu(t) = -2\pi d\mu_0 f_\mathrm{d} \cos(2\pi f_\mathrm{d} t) \int_\Omega \left\langle \boldsymbol{\varrho}_\nu(\boldsymbol{r}), \boldsymbol{e}_\alpha \right\rangle \bar{\mathrm{m}}'\left(2g \left| \langle \boldsymbol{e}_\alpha, \boldsymbol{r}\rangle - \tfrac{d}{2g}\sin(2\pi f_\mathrm{d} t)\right|\right) c(\boldsymbol{r})\,\mathrm{d}\boldsymbol{r}.$$

The vector $\boldsymbol{e}_\alpha^\perp = (\cos\frac{\alpha}{2}, \sin\frac{\alpha}{2}, 0)$ is perpendicular to $\boldsymbol{e}_\alpha$ in the xy plane. With the basis vectors $\boldsymbol{e}_\alpha$ and $\boldsymbol{e}_\alpha^\perp$, we can write every point $\boldsymbol{r}$ in the xy-plane as $\boldsymbol{r} = s\boldsymbol{e}_\alpha + w\boldsymbol{e}_\alpha^\perp$. Using Fubini's theorem, we rewrite the bivariate integral above as the iterated integral

$$u_\nu(t) = -2\pi d\mu_0 f_\mathrm{d} \cos(2\pi f_\mathrm{d} t) \int_\Omega \left\langle \boldsymbol{\varrho}_\nu(s,w), \boldsymbol{e}_\alpha \right\rangle \bar{\mathrm{m}}'\Big(2g \left| s - \tfrac{d}{2g}\sin(2\pi f_\mathrm{d} t)\right|\Big) c(s,w)\,\mathrm{d}s\,\mathrm{d}w.$$

Assuming that the coil sensitivity is constant $\boldsymbol{\varrho}_\nu(\boldsymbol{r}) = \boldsymbol{\varrho}_\nu$, this equation simplifies to

$$\begin{aligned} u_\nu(t) &= -2\pi d\mu_0 f_\mathrm{d} \cos(2\pi f_\mathrm{d} t) \left\langle \boldsymbol{\varrho}_\nu, \boldsymbol{e}_\alpha \right\rangle \int_\mathbb{R} \bar{\mathrm{m}}'\left(2g \left| s - \tfrac{d}{2g}\sin(2\pi f_\mathrm{d} t)\right|\right) \int_\mathbb{R} c(s,w)\,\mathrm{d}w\,\mathrm{d}s \\ &= -2\pi d\mu_0 f_\mathrm{d} \cos(2\pi f_\mathrm{d} t) \left\langle \boldsymbol{\varrho}_\nu, \boldsymbol{e}_\alpha \right\rangle \int_\mathbb{R} \bar{\mathrm{m}}'\left(2g \left| s - \tfrac{d}{2g}\sin(2\pi f_\mathrm{d} t)\right|\right) \mathcal{R}c(\boldsymbol{e}_\alpha, s)\,\mathrm{d}s, \end{aligned}$$

where $\mathcal{R}c(\boldsymbol{e}_\alpha, s)$ denotes the Radon transform of c for the line given by $\langle \boldsymbol{r}, \boldsymbol{e}_\alpha\rangle = s$. For an ideal non-rotating FFL we can therefore recover the following imaging model originally stated in [19, Theorem 1].

Corollary 4.2. *Let $\bar{\mathrm{m}} : \mathbb{R} \to \mathbb{R}$ be odd and twice continuously differentiable, and let $\boldsymbol{B}(\boldsymbol{r},t)$ be the magnetic field generating an ideal non-rotating FFL as derived in Section 3.2. Then, the imaging equation* (8) *in Theorem 4.1 simplifies to*

$$u_\nu(t) = -2\pi d\mu_0 f_\mathrm{d} \cos(2\pi f_\mathrm{d} t) \left\langle \boldsymbol{\varrho}_\nu, \boldsymbol{e}_\alpha \right\rangle \Big(\bar{\mathrm{m}}'(|2g\cdot|) * \mathcal{R}c(\boldsymbol{e}_\alpha, \cdot)\Big)\big(\tfrac{d}{2g}\sin\big(2\pi f_\mathrm{d} t\big)\big), \quad (10)$$

where $*$ denotes the standard one-dimensional convolution between the kernel function $\bar{\mathrm{m}}'(|2gs|)$ and the Radon transform $\mathcal{R}c(\boldsymbol{e}_\alpha, s)$ with respect to the second variable s.

Remark 1. Formula (10) provides a direct way to reconstruct the particle concentration c from the voltage signal u_ν [1, 3, 6, 19]. Dividing the voltage signal u_ν by the velocity and sensitivity factor $-2\pi d\mu_0 f_\mathrm{d} \cos(2\pi f_\mathrm{d} t)\left\langle \boldsymbol{\varrho}_\nu, \boldsymbol{e}_\alpha \right\rangle$ and regridding the so obtained time signal onto the interval $[-\frac{d}{2g}, \frac{d}{2g}]$, we get an expression for $(\bar{\mathrm{m}}'(|2g\cdot|) * \mathcal{R}c(\boldsymbol{e}_\alpha, \cdot))(s)$. Deconvolution then yields the Radon transform $\mathcal{R}c(\boldsymbol{e}_\alpha, s)$ of the concentration c. By applying the filtered back projection (FBP) to the Radon data $\mathcal{R}c(\boldsymbol{e}_\alpha, s)$ we finally can reconstruct c. Note that in some works, the deconvolution step is omitted in the reconstruction, see [21].

Remark 2. For a rotating FFL as given in Section 3.1, the imaging equation (9) leads to the same formula (10), with the only difference that the fixed angle α is replaced with the rotating angle $\alpha(t) = 2\pi f_\mathrm{rot} t$. Note that in this case the parallelity assumption of Theorem 4.1 is not satisfied. However, if $f_\mathrm{d} >> f_\mathrm{rot}$, parallelity of the magnetic field $\boldsymbol{B}(\boldsymbol{r},t)$ to its velocity field is almost given and the simplified imaging equation (9) provides a good approximation to the general imaging equation (1).

4.3. An approximative model for realistic magnetic fields

Apart from the ideal FFL and 1D-FFP imaging setups described in the previous Section 4.2 and in the appendix (Section 8.3), no analytic inversion formulas for the reconstruction of the particle distribution c are known. Our imaging equation (9) allows to derive a discrete MPI model for a much wider class of imaging setups, provided that the magnetic fields are (approximately) parallel to its velocity field. In particular, this allows us to incorporate more complex magnetic fields and to reconstruct the particle density c algebraically from a modelled system matrix.

As a first step towards a discretization of the integral in (9), we approximate the derivative $\bar{\mathrm{m}}'(x)$ for $0 \leq x < b$ using a piecewise constant function and a threshold $b > 0$. The energy of the function $\bar{\mathrm{m}}'$ is in general concentrated in a small region around the origin. In this way, $\bar{\mathrm{m}}'(|\boldsymbol{B}(\boldsymbol{r},t)|)$ gets essentially large only in the low-field volume (LFV) of the magnetic field $\boldsymbol{B}(\boldsymbol{r},t)$, i.e., in those regions in which the modulus $|\boldsymbol{B}(\boldsymbol{r},t)|$ is small. The chosen threshold $b > 0$ therefore gives a bound for the LFV of $\boldsymbol{B}(\boldsymbol{r},t)$ in which $\bar{\mathrm{m}}'$ is large enough to give an impact for the integral equation (9).

In the following, we restrict our attention to the approximation of the function $\bar{\mathrm{m}}'$ in the positive interval $[0,b)$. We consider N nodes $0 < x_1 < \cdots < x_N < b$ and set $x_{N+1} = b$, $x_0 = 0$. The approximation of $\bar{\mathrm{m}}'$ with piecewise constant functions is defined on the intervals $I_n = [x_n, x_{n+1})$, $n = 0, \ldots, N$. We construct

$$\bar{\mathrm{m}}'_N(x) = \sum_{n=0}^{N} s_n \chi_{I_n}(x) \tag{11}$$

in such a way that $\lim_{N\to\infty} \bar{\mathrm{m}}'_N(x) = \bar{\mathrm{m}}'(x)$ for all $x \in [0,b)$. Here, the indicator function χ_{I_n} is defined as $\chi_{I_n}(x) = 1$ if $x \in I_n$ and $\chi_{I_n}(x) = 0$ if $x \notin I_n$. Two schemes to obtain the nodes x_n and the values s_n, $n = 0, \ldots, N$, are given in Section 5 (we will use the Langevin function (3) to model $\bar{\mathrm{m}}$). This construction allows us to approximate the time-derivative of the magnetization derived in (8) with a piecewise constant function:

$$\begin{aligned}
\bar{\mathrm{m}}'_N(|\boldsymbol{B}(\boldsymbol{r},t)|)\,\frac{\mathrm{d}}{\mathrm{d}t}\boldsymbol{B}(\boldsymbol{r},t) &= \begin{cases} s_n\,\dfrac{\mathrm{d}}{\mathrm{d}t}\boldsymbol{B}(\boldsymbol{r},t) & \text{if } |\boldsymbol{B}(\boldsymbol{r},t)| \in I_n, \\ \boldsymbol{0} & \text{if } |\boldsymbol{B}(\boldsymbol{r},t)| \geq b \end{cases} \\
&= \sum_{n=0}^{N} s_n\,\chi_{I_n}(|\boldsymbol{B}(\boldsymbol{r},t)|)\,\frac{\mathrm{d}}{\mathrm{d}t}\boldsymbol{B}(\boldsymbol{r},t).
\end{aligned}$$

Using the approximate derivative $\bar{\mathrm{m}}'_N$ instead of $\bar{\mathrm{m}}'$, the imaging equation given in equation (9) can be written as

$$u_\nu(t) = -\mu_0 \sum_{n=0}^{N} s_n \int_{F_n(t)} \left\langle \boldsymbol{\varrho}_\nu(\boldsymbol{r}), \frac{\mathrm{d}}{\mathrm{d}t}\boldsymbol{B}(\boldsymbol{r},t) \right\rangle c(\boldsymbol{r})d\boldsymbol{r}, \tag{12}$$

where

$$F_n(t) = \{\boldsymbol{r} \in \Omega \mid |\boldsymbol{B}(\boldsymbol{r},t)| \in I_n\}. \tag{13}$$

Introducing the kernel functions

$$K_\nu(\boldsymbol{r},t) = -\mu_0 \left\langle \boldsymbol{\varrho}_\nu(\boldsymbol{r}), \frac{\mathrm{d}}{\mathrm{d}t}\boldsymbol{B}(\boldsymbol{r},t) \right\rangle,$$

we finally obtain the integral equation

$$u_\nu(t) = \sum_{n=0}^{N} s_n \int_{F_n(t)} K_\nu(\boldsymbol{r},t)c(\boldsymbol{r})d\boldsymbol{r}. \tag{14}$$

We have the following limiting relation between the approximate model (14) and the orignal equation (9).

Theorem 4.3. *Let* $\operatorname{supp} c = \Omega \subset \mathbb{R}^3$ *be a compact set. For* $t \geq 0$*, let the function* $K_\nu(\boldsymbol{r},t)c(\boldsymbol{r})$ *be integrable over* Ω *and* $\bar{\mathrm{m}}$ *be twice continuously differentiable. Set* $b > 0$ *such that*

$$\max_{\boldsymbol{r}\in\Omega} |B(\boldsymbol{r},t)| < b.$$

Let $\bar{\mathrm{m}}'_N$ *be an approximation of* $\bar{\mathrm{m}}'$ *given in* (11) *such that* $\lim_{N\to\infty} \bar{\mathrm{m}}'_N(x) = \bar{\mathrm{m}}'(x)$ *uniformly on* $[0,b)$*. Then, we have*

$$\lim_{N\to\infty} \sum_{n=0}^{N} s_n \int_{F_n(t)} K_\nu(\boldsymbol{r},t)c(\boldsymbol{r})d\boldsymbol{r} = \int_\Omega \bar{\mathrm{m}}'(|B(\boldsymbol{r},t)|)K_\nu(\boldsymbol{r},t)c(\boldsymbol{r})d\boldsymbol{r}.$$

Proof. If $\bar{\mathrm{m}}$ is twice continuously differentiable, Theorem 5.1 below together with one of the node selection strategies given in Section 5.2 guarantees the existence of a piecewise uniform approximation $\bar{\mathrm{m}}'_N$ of $\bar{\mathrm{m}}'$ on the interval $[0,b)$. In fact, Theorem 5.1 shows that both constructions given in Section 5.1 are adequate. The domain Ω corresponds to the disjoint union $\bigcup_{n=0}^{N} F_n(t)$ and the uniform convergence of $\bar{\mathrm{m}}'_N$ yields

$$\begin{aligned}\lim_{N\to\infty} \sum_{n=0}^{N} s_n \int_{F_n(t)} K_\nu(\boldsymbol{r},t)c(\boldsymbol{r})d\boldsymbol{r} &= \lim_{N\to\infty} \int_\Omega \sum_{n=0}^{N} s_n \chi_{I_n}(|\boldsymbol{B}(\boldsymbol{r},t)|)K_\nu(\boldsymbol{r},t)c(\boldsymbol{r})d\boldsymbol{r} \\ &= \int_\Omega \bar{\mathrm{m}}'(|B(\boldsymbol{r},t)|)K_\nu(\boldsymbol{r},t)c(\boldsymbol{r})d\boldsymbol{r}.\end{aligned}$$

□

We will use the approximate imaging equation given in (14) to obtain a model-based algebraic reconstruction formula. We can regard (14) however also as an approximative MPI imaging model in case that the magnetic field $\boldsymbol{B}(\boldsymbol{r},t)$ is, as in Theorem 4.1, parallel to its velocity field.

5. Numerical implementation of the new model

5.1. Piecewise linear approximation of the magnetization function $\bar{\mathrm{m}}$

In this section, we shortly provide two ways on how to approximate the magnetization function $\bar{\mathrm{m}}$ with a piecewise linear function $\bar{\mathrm{m}}_N$, and, at the same time, on how to approximate the derivative $\bar{\mathrm{m}}'$ with a piecewise constant function $\bar{\mathrm{m}}'_N$. The approximation $\bar{\mathrm{m}}_N$ on the positive half-axis consists of a polygon with $N+2$ linear polynomials. For this, we consider N nodes $0 < x_1 < \cdots < x_N < b$ and set $x_{N+1} = b$, $x_0 = 0$. The linear polynomials are defined on the intervals $I_n = [x_n, x_{n+1})$, $n = 0,\ldots,N$, and on $I_{N+1} = [x_{N+1},\infty)$.

1) (Secant approximation scheme) For $n \in \{0, \dots, N\}$, set

$$s_n = \frac{\bar{\mathrm{m}}(x_{n+1}) - \bar{\mathrm{m}}(x_n)}{x_{n+1} - x_n}.$$

2) (Tangent approximation scheme) For $n \in \{0, \dots, N\}$, set

$$s_n = \begin{cases} \bar{\mathrm{m}}'(0) & \text{if } n = 0, \\ \bar{\mathrm{m}}'(\frac{x_{n+1}+x_n}{2}) & \text{if } n > 0. \end{cases}$$

For both choices, we get for $x \geq 0$ the following approximants for the magnetization $\bar{\mathrm{m}}$ and its derivative $\bar{\mathrm{m}}'$:

$$\bar{\mathrm{m}}'_N(x) = \sum_{n=0}^{N} s_n \chi_{I_n}(x), \quad \bar{\mathrm{m}}_N(x) = \int_0^x \sum_{n=0}^{N} s_n \chi_{I_n}(y) dy.$$

An illustration of the approximation $\bar{\mathrm{m}}_N$ for the secant scheme is shown in Fig. 2. For negative x, we expand $\bar{\mathrm{m}}_N$ and $\bar{\mathrm{m}}'_N$ such that $\bar{\mathrm{m}}_N$ is odd and $\bar{\mathrm{m}}'$ is even on $\mathbb{R}$, i.e.,

$$\bar{\mathrm{m}}'_N(x) = \bar{\mathrm{m}}'_N(-x), \qquad \bar{\mathrm{m}}_N(x) = -\bar{\mathrm{m}}_N(-x) \qquad \text{for } x \in \mathbb{R}.$$

Example 5.1. For the tangent scheme, we obtain a simple approximation of the derivative $\bar{\mathrm{m}}'$ already for $N = 0$. In this case, using the Langevin model (3) to describe $\bar{\mathrm{m}}$ and formula (4) for the derivative, we get the approximation

$$\bar{\mathrm{m}}'_N(x) = \begin{cases} \dfrac{m_0 \lambda}{3}, & 0 \leq x < b, \\ 0, & x \geq b. \end{cases} \tag{15}$$

Then, if

$$F_0(t) = \{\boldsymbol{r} \in \mathbb{R}^3 : \ |\boldsymbol{B}(\boldsymbol{r}, t)| < b\}$$

denotes the LFV at time t in which the modulus of the magnetic field is smaller than b, we obtain in (14) the simple integral equation

$$u_\nu(t) = -\frac{\mu_0 m_0 \lambda}{3} \int_{F_0(t)} \left\langle \boldsymbol{\varrho}_\nu(\boldsymbol{r}), \frac{\mathrm{d}}{\mathrm{d}t} \boldsymbol{B}(\boldsymbol{r}, t) \right\rangle \, c(\boldsymbol{r}) \, d\boldsymbol{r},$$

i.e., the voltage signal u_ν is approximately generated by integrating the particle density together with the velocity term $\left\langle \boldsymbol{\varrho}_\nu(\boldsymbol{r}), \frac{\mathrm{d}}{\mathrm{d}t} \boldsymbol{B}(\boldsymbol{r}, t) \right\rangle$ over the LFV $F_0(t)$.

Theorem 5.1. *If $\bar{\mathrm{m}}$ is twice continuously differentiable then, for both, the tangent and the secant approximation scheme, we have the properties:*

$$\sup_{x \in [0,b)} |\bar{\mathrm{m}}'(x) - \bar{\mathrm{m}}'_N(x)| \leq \sup_{x \in [0,b)} |\bar{\mathrm{m}}''(x)| \max_{n \in \{0,\dots,N\}} (x_{n+1} - x_n), \tag{16}$$

$$\sup_{x \in [0,b)} |\bar{\mathrm{m}}(x) - \bar{\mathrm{m}}_N(x)| \leq \sup_{x \in [0,b)} |\bar{\mathrm{m}}''(x)| \sum_{n=0}^{N} (x_{n+1} - x_n)^2. \tag{17}$$

Proof. For both, the tangent and the secant scheme, the mean value theorem provides for $x \in I_n$ the estimate

$$|\bar{\mathrm{m}}'(x) - \bar{\mathrm{m}}'_N(x)| \leq \sup_{\xi \in I_n} |\bar{\mathrm{m}}''(\xi)| (x_{n+1} - x_n).$$

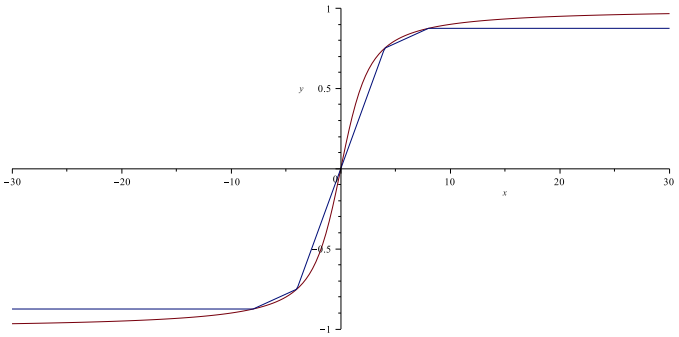

Figure 2: Piecewise approximation of the Langevin function L by the secant scheme with $N = 1$, extended point-symmetrically to the negative axis.

This immediately implies (16). We can use this estimate also to obtain (17):

$$|\bar{\mathrm{m}}(x) - \bar{\mathrm{m}}_N(x)| = \left| \int_0^x (\bar{\mathrm{m}}'(x) - \bar{\mathrm{m}}'_N(x))\,\mathrm{d}x \right| \le \sum_{n=0}^{N} \int_{I_n} |\bar{\mathrm{m}}'(x) - \bar{\mathrm{m}}'_N(x)|\,\mathrm{d}x$$
$$\le \sup_{\xi\in[0,b)} |\bar{\mathrm{m}}''(\xi)| \sum_{n=0}^{N} (x_{n+1} - x_n)^2. \tag{18}$$

□

5.2. Selection of the nodes

The nodes $x_1, \ldots, x_N$ in the interval $(0, b)$ can be chosen in several different ways. Based on our result in Theorem 5.1, we provide two simple options:

1) Equidistant points (the simplest choice):

$$x_n = \frac{b\,n}{N+1}, \qquad n \in \{0, \ldots, N+1\}.$$

2) L_1-optimal points: choose $x_1, \ldots, x_N$ in $(0, b)$ such that the L^1-norm

$$\int_0^b |\bar{\mathrm{m}}'(x) - \bar{\mathrm{m}}'_N(x)|\,\mathrm{d}x$$

is minimized.

Theorem 5.1 ensures that both choices lead to a uniform convergence of $\bar{\mathrm{m}}'_N$ towards $\bar{\mathrm{m}}'$ on the interval $[0, b)$. The L_1-optimized variant yields a better approximation quality for the derivative $\bar{\mathrm{m}}'$ as well as for the magnetization function $\bar{\mathrm{m}}$. This can be seen particularly in the estimate (18), in which an L_1-optimal ensemble makes the second inequality redundant.

In case of the tangent scheme, we give an explicit formula for the L_1-norm. We assume that the derivative $\bar{\mathrm{m}}'$ is positive and strictly monotonically decreasing when

$x \geq 0$, and $\bar{\mathrm{m}}(0) = 0$. This is indeed the case if the magnetization $\bar{\mathrm{m}}$ is given as in (3) by the Langevin model. Then, we get the explicit formula

$$\begin{aligned}
\int_0^b |\bar{\mathrm{m}}'(x) - \bar{\mathrm{m}}'_N(x)|\,\mathrm{d}x &= \sum_{n=0}^{N} \int_{I_n} |\bar{\mathrm{m}}'(x) - s_n|\,\mathrm{d}x \\
&= \int_{I_0} |\bar{\mathrm{m}}'(x) - \bar{\mathrm{m}}'(0)|\,\mathrm{d}x + \sum_{n=1}^{N} \int_{I_n} |\bar{\mathrm{m}}'(x) - \bar{\mathrm{m}}'\left(\tfrac{x_n+x_{n+1}}{2}\right)|\,\mathrm{d}x \\
&= \bar{\mathrm{m}}'(0)x_1 - \bar{\mathrm{m}}(x_1) + \sum_{n=1}^{N} \left(\int_{x_n}^{\frac{x_n+x_{n+1}}{2}} \bar{\mathrm{m}}'(x)\,\mathrm{d}x - \int_{\frac{x_n+x_{n+1}}{2}}^{x_{n+1}} \bar{\mathrm{m}}'(x)\,\mathrm{d}x \right) \\
&= \bar{\mathrm{m}}'(0)x_1 + \sum_{n=1}^{N} 2\left(\bar{\mathrm{m}}(\tfrac{x_n+x_{n+1}}{2}) - \bar{\mathrm{m}}(x_n) \right) - \bar{\mathrm{m}}(x_{N+1}) = F(x_1, \ldots, x_N).
\end{aligned}$$

Thus, in order to find the ensemble in which the L^1-norm gets minimal, we only have to minimize the functional F.

5.3. Full discretization and model-based imaging matrix

We assume to have T discrete time measurements $\boldsymbol{u}_\nu = (u_\nu(t_1), \ldots, u_\nu(t_T))$ of the voltage signal u_ν. To discretize the particle density $c(\boldsymbol{r})$, we use the representation

$$c(\boldsymbol{r}) = \sum_{k=1}^{K} c_k \delta_k(\boldsymbol{r})$$

of c in a given set of basis functions δ_k, $k = 1, \ldots, K$. The approximate model equation stated in (12) can now be discretized as

$$u_\nu(t_j) = \sum_{n=0}^{N} s_n \sum_{k=1}^{K} c_k \int_{F_n(t_j)} K_\nu(\boldsymbol{r}, t_j)\delta_k(\boldsymbol{r})d\boldsymbol{r}.$$

We denote by $S_{\nu,n} \in \mathbb{R}^{T\times K}$ the rectangular matrix with the entries

$$(S_{\nu,n})_{j,k} = \int_{F_n(t_j)} K_\nu(\boldsymbol{r}, t_j)\delta_k(\boldsymbol{r})d\boldsymbol{r}$$

Then, a model-based discrete imaging equation to recover the particle concentration can be written as

$$\boldsymbol{u}_\nu = \left(\sum_{n=0}^{N} s_n S_{\nu,n} \right) \boldsymbol{c} = S_\nu \boldsymbol{c}, \tag{19}$$

where $\boldsymbol{c} = (c_1, \ldots, c_K)$ and $S_\nu \in \mathbb{R}^{T\times K}$ is the modelled system matrix for the receive coil ν. In our implementation, we sample the concentration $c(\boldsymbol{r})$ with a Dirac comb such that $c_k = c(\boldsymbol{r}_k)$ are the sought concentration values at the positions $\boldsymbol{r}_k$ and the system matrix entries $(S_{\nu,n})_{j,k}$ are given by

$$(S_{\nu,n})_{j,k} = \begin{cases} K_\nu(\boldsymbol{r}_k, t_j) & \text{if } \boldsymbol{r}_k \in F_n(t_j), \\ 0 & \text{otherwise.} \end{cases}$$

5.4. Algebraic reconstruction of the particle concentration

In order to solve the system of equations (19) for the particle concentration $\boldsymbol{c}$, we combine the information of all V receive coils. In this way, we get the system

$$\underbrace{\begin{pmatrix} \boldsymbol{u}_1 \\ \vdots \\ \boldsymbol{u}_V \end{pmatrix}}_{\boldsymbol{u}} = \underbrace{\begin{pmatrix} S_1 \\ \vdots \\ S_V \end{pmatrix}}_{S} \boldsymbol{c}.$$

From this system we extract the particle concentration $\boldsymbol{c}$ by calculating the solution of the normal equation $S^T S\boldsymbol{c} = S^T \boldsymbol{u}$ iteratively using the LSQR algorithm [23] together with an early stopping rule.

Remark 3. Although the particle reconstruction in MPI is in general an ill-posed inverse problem [5, 14, 22], at that stage, we did not incorporate additional regularization for the solution of the linear system $\boldsymbol{u} = S\boldsymbol{c}$. The various discretization steps applied in our model and the early stopping of the LSQR procedure already provide a certain regularization of the problem. In combination with our model, one could of course apply also more advanced regularization schemes as for instance described in [28].

6. Experiments

Based on the phantom presented in Fig. 3(a), two types of magnetic field topologies are used to study the influence on the reconstruction: an ideal rotating FFL magnetic field, represented by a few low-degree spherical harmonics, as described in Section 3.1; and a realistic one, obtained either from a realistic numerical model of the magnetic coil or from measurements. A concrete example of such a realistic field is given in Section 3.3.

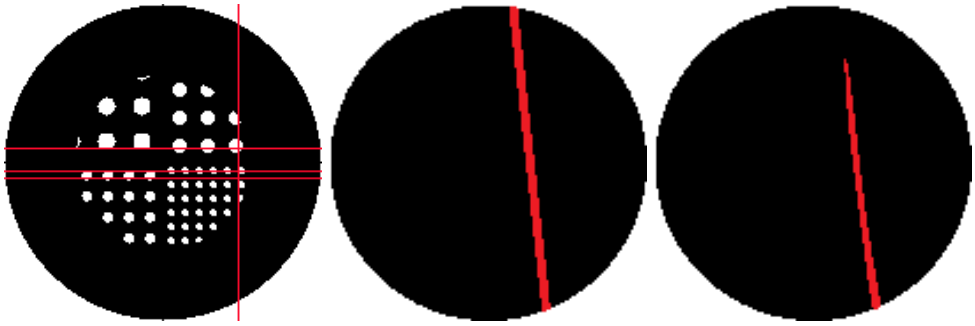

(a) (b) (c)

Figure 3: Ideal and realistic rotating FFL's: (a) A phantom composed of circles (in white) of 4, 6, 8 and 10 mm diameter inside a 100 mm diameter circle. This phantom is placed inside a 173 mm diameter imaging area. The reconstructions along the illustrated horizontal (Top: 1st line, bottom: 3rd line) and vertical (4th line) lines are shown in Fig. 9, 11 and 13. (b) and (c) show the LFV (in red) with a field amplitude smaller than 2 mT for an ideal and a realistic field topology, respectively (f_{rot}=100 Hz).

The influence of the higher degree spherical harmonics on the LFV can be observed by comparing Fig. 3(b) which illustrates the LFV at 2 mT for ideal topologies at a given time $t = 17.25$ μs in our sequence, with Fig. 3(c) which shows the corresponding LFV for the realistic field topology used afterwards in our simulations. The LFV compared to an ideal FFL is slightly bended and interrupted on the upper part. To highlight the effect of these differences on the reconstructed particle concentrations, we run now experiments comparing side by side the images obtained either by a filtered back-projection (FBP) for ideal and realistic fields or by our algebraic reconstruction procedure (cf. Subsection 5.4).

6.1. General experimental parameters

The modelled FFL scanner uses the same coils to move the FFL and to receive the signals used for the reconstruction. Those two coils are the drive coils. For all the presented results, the drive field frequency is fixed at f_{d}=25 kHz and the line rotation frequency f_{rot} is varied from 100 Hz to 1000 Hz. Due to the RAM limitation of 1 TB in our system, a rotation frequency of 10 Hz has not be conducted. 250 and 25 projections were used for the 100 Hz and 1000 Hz reconstruction, respectively. It is common to set the drive frequency between <1 kHz and 150 kHz, and the rotation frequency from <1 Hz to 100 Hz. The sampling frequency is set to 8 Mhz (4 Mhz for FBP), thus obtaining 160 points per projection (80 for FBP) and emulating the common properties of the acquisition hardware used. Note that in order to do a frequency filtering on the measured signal, the whole rotation was always simulated to obtain a perfectly resolved spectra. Indeed, the hardware of an actual MPI scanner always filters out a frequency range around f_{d}. To reproduce this effect, we always removed all the information below 1.4 f_{d} from the measured signal. Furthermore, a Gaussian noise was added to all simulations. For the signal simulation, a spatial discretization of $1 \times 1 \times 1$ mm^3 was used, whereas a discretization of $1.3 \times 1.3 \times 1$ mm^3 was used for the system matrix. The solution of the proposed discretized MPI model (19) was solved using Matlab's LSQR implementation, which was always stopped after 20 iterations. This has been optimized by visual inspection in a simulation using a rotation frequency f_{rot} of 100 Hz, a threshold of $b = 10$ mT and kept constant for all further tests.

6.2. Comparison with the filtered back projection

We compare our method with the filtered back projection (FBP), which is commonly used for FFL systems to perform the image reconstruction [1, 21]. The FBP implementation of Matlab (Version 7.11.0) was used to performed the first test. The Radon projections are obtained by the reconstruction steps described in Remark 1, using half a period of a drive field sweep with frequency f_{d} for fixed approximate angles $\alpha \approx 2\pi f_{\mathrm{rot}} t$ and for discrete values of the displacement variable $s = \frac{d}{2g} \sin\left(2\pi f_{\mathrm{d}} t\right)$ in a subinterval of $[-\frac{d}{2g}, \frac{d}{2g}]$. The so obtained Radon data is assembled into a sinogram and then reconstructed using the FBP algorithm. The reconstruction results for the FBP applied to ideal and realistic FFL topologies are displayed in Fig. 5 and Fig. 6. Note that, as we use approximate fixed angles α for the Radon projections, the continuous rotation of the FFL in a drive field sweep causes rotation artifacts in the FBP reconstructions that have to be corrected. This is in particular visible for $f_{\mathrm{rot}} = 1000$ Hz.

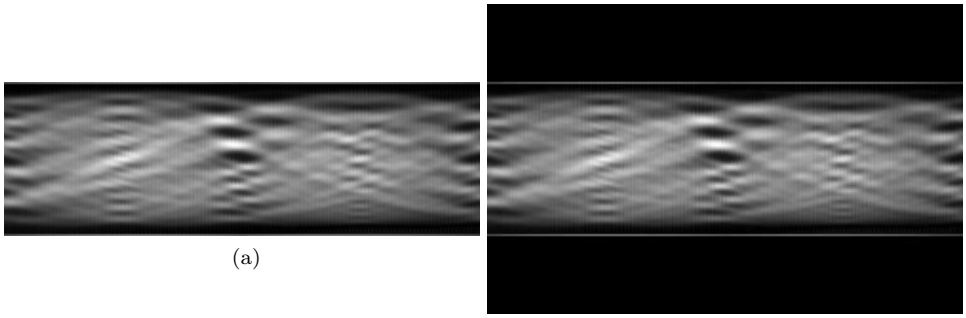

(a) (b)

Figure 4: Two sinograms of the phantom from Fig. 3(a) for an ideal FFL topology with $f_{\text{rot}} = 100$ Hz used as input data for the FBP. (a) Sinogram of a phantom in which the maximal displacement of the Radon transform is adapted to the support of the phantom. It is used to generate the reconstruction shown in Fig. 5 (row 1, left). (b) Same sinogram padded with zero, to increase the reconstruction area of the FBP.

The sinogram obtained using the ideal model of a rabbit sized FFL MPI scanner [3] is illustrated in Fig. 4(a). To fully asses the differences between the reconstruction methods over the whole scanner opening, we additionally pad this ideal sinogram with zeros, as shown in Fig. 4(b).

The results of the FBP reconstructions are compared with the images obtained by our method. The system matrix S_ν for the algebraic reconstruction in (19) is constructed using the threshold $b = 10$ mT and the secant approximation scheme with $N = 30$ equidistant nodes for the discretization of the Langevin function. The information about the magnetic field $\boldsymbol{B}(\boldsymbol{r}, t)$ and its time-derivative is obtained by measurements or simulations.

Fig. 5 and Fig. 6 highlight the main advantages of our method. Indeed, the presented model-based reconstruction method compensates the main artifacts introduced by the idealized assumptions in the FBP reconstruction. The rotation artifacts which appear in all images produced by the FBP and which are (independently of the field complexity) only linked to the continuous rotation of the LFV during an acquisition are compensated in our method. The distortion artifacts visible in both Fig. 5 and Fig. 6, introduced by the more complex realistic field topology, are also corrected. In particular, this can be observed by the corrected geometric distances between two points of the phantom.

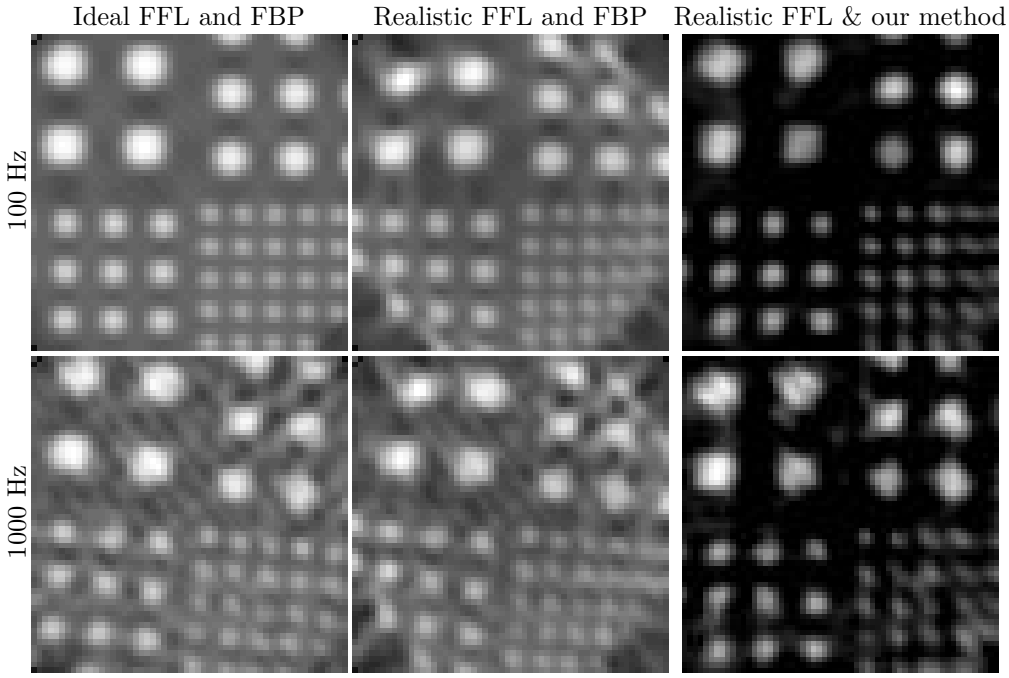

Figure 5: Comparison of reconstructions for different rotating FFL topologies using $f_{\text{rot}} = 100$ Hz (1. row), $f_{\text{rot}} = 1000$ Hz (2. row), and identically chosen fields of view.

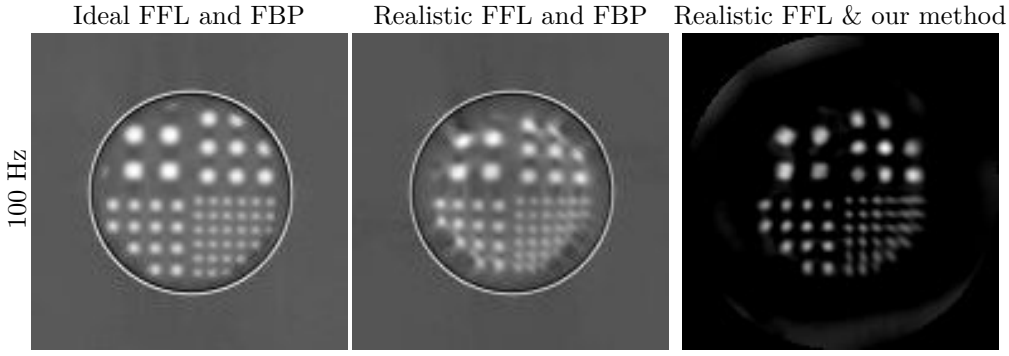

Figure 6: Reconstructions of Fig. 5 (first row) using an enlarged field of view. A sinogram padded with zero, as illustrated in Fig. 4b, extends the reconstruction area of the FBP.

We would like to point out that the ring artifacts in Fig. 6 (left and middle) are produced by the FBP algorithm as a consequence of erroneous Radon data at the upper and lower boundary of the sinogram. These boundary errors stem from numerical issues that arise during the recovery of the Radon data $\mathcal{R}c(\boldsymbol{e}_\alpha, s)$ from the voltage signals $u_\nu(t)$ as described in Corollary 4.2 and Remark 1. Namely, this recovery gets ill-conditioned when the velocity of the FFL tends to zero, which is the case at the boundary of the field of view. This is particularly evident in the zero

padded sinogram displayed in Fig. 4(b). The two visible horizontal grey lines (which are also present in the Fig. 4(a) mark these singularities which in turn lead to the production of ring artifacts by the FBP algorithm, see e.g. [2]. A closer look at the left and center images in Fig. 6 shows that there are high oscillations around the ring artifacts (including negative grey values) that lead to a wrong background color. Interestingly, our algebraic reconstruction method seems to avoid such artifacts which is why the reconstructions appear without any background signal. The reason why the ring artifacts are not produced in our reconstructions may be a consequence of our improved model and the use of an iterative (regularized) reconstruction procedure.

6.3. Influence of amplitude threshold

We further study the influence of the threshold b on the reconstruction quality. In Fig. 7 we can see how this threshold determines the volume of the LFV used in the discrete imaging equation (19) to model the generation of the MPI signal.

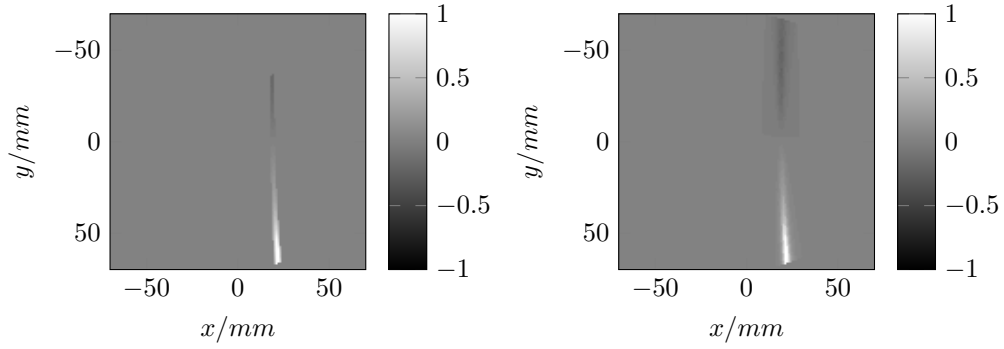

Figure 7: Influence of the threshold b on the information included in the system matrix S_ν for f_{rot}=100 Hz at t=17.25 μs using the secant approximation scheme with $N = 30$ equidistant nodes. The normalized entries of the system function S_ν are displayed: (a) for a threshold of $b = 2$ mT and (b) for a threshold of $b = 10$ mT.

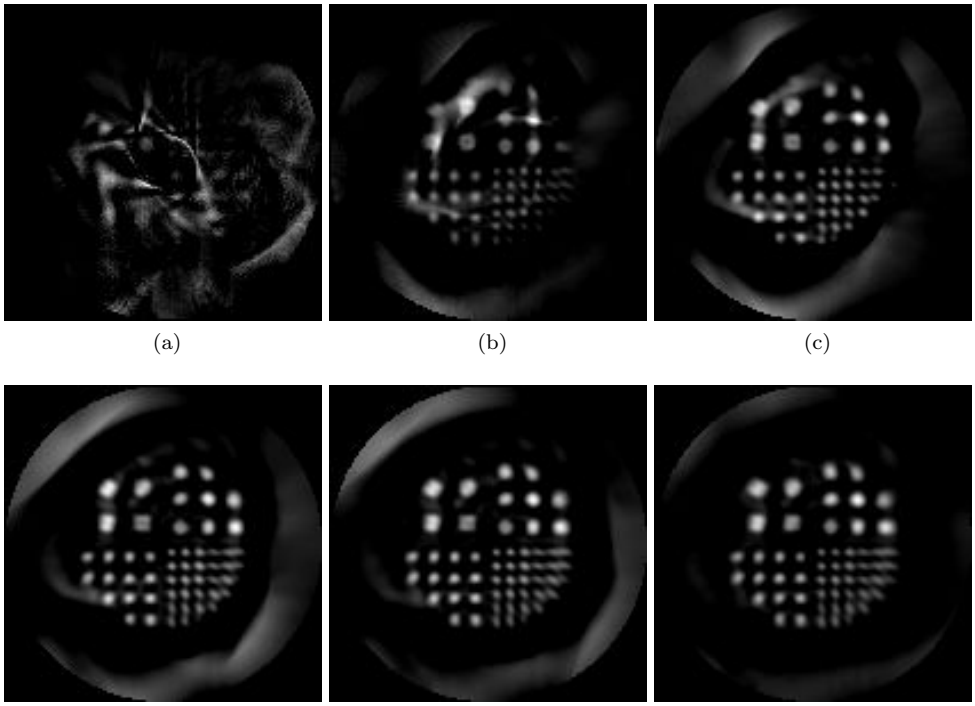

(a) (b) (c)

(d) (e) (f)

Figure 8: Reconstructions with a threshold b equal to $1, 2, 3, 4, 5$ and 10 mT.

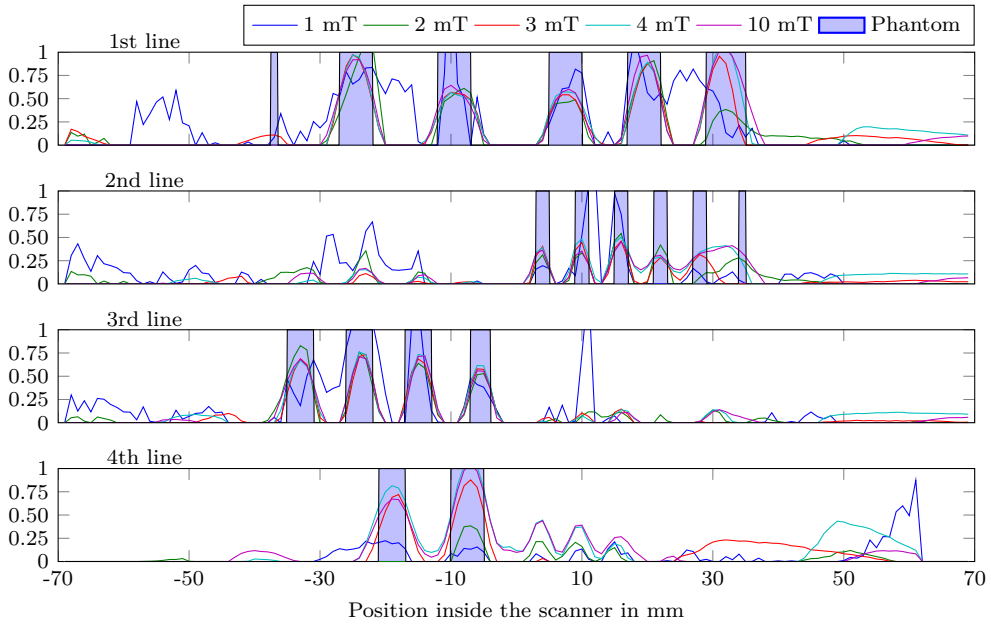

Figure 9: Comparison of the line profiles (as shown in Fig. 3(a)) for the reconstructions obtained with our method using different thresholds b and the original phantom.

We consider again the example of the phantom given in Fig. 3, with f_{rot}=100 Hz, and using the secant approximation scheme with $N = 30$ for the Langevin function. The reconstructions in Fig. 8 and the line profiles in Fig. 9 show that the choice of the threshold b has a strong impact on the reconstruction quality in the entire field of view (FOV) when b is in the range 1 to 4 mT. On the other hand, if b is between 4 and 10 mT only small differences are visible on the periphery of the FOV. Thus, in this example a threshold b of 10 mT is sufficient, and a threshold of 4 mT yields already very good results for the central part of the FOV. Note that a smaller threshold is desirable from a computational point of view in order to benefit from a sparser representation of the system matrix S_ν. We also remark that for all six thresholds the same reconstruction technique based on the LSQR algorithm with early stopping at 20 iterations was used. Adapting the number of iterations for each b or using additional regularization strategies can improve the reconstruction quality for the single thresholds even further. In this way, a threshold of $b = 3$ might already be sufficient for a reasonable reconstruction or the pincushion artifacts at the boundaries of Fig. 8(e) and 8(f) might vanish.

6.4. Discretization effects

In two additional tests, we study discretization effects on the reconstruction. In the first test, we search for the optimal number of equidistant nodes N for the piecewise approximation of the Langevin function in the tangential approximation scheme on an example with f_{rot}=100 Hz and a threshold $b = 10$ mT. The corresponding results are illustrated in Fig. 10 and Fig. 11. It is visible that already for $N = 8$ the piecewise approximation of the Langevin function provides acceptable reconstructions.

In a second experiment, we test three different discretization techniques for the Langevin function on an example with f_{rot}=100 Hz, threshold $b = 10$ mT and $N = 30$ nodes. As shown in Fig. 12 and Fig. 13, all three discretizations provide comparable reconstruction results.

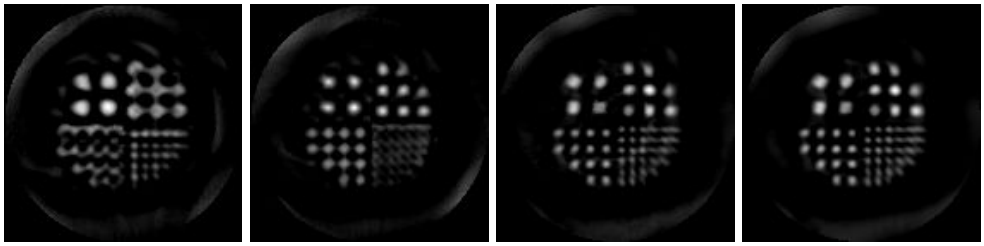

(a) (b) (c) (d)

Figure 10: Reconstruction with different number N of nodes in the discretization of the Langevin function (tangential approximation scheme, $b = 10$ mT). The results for 3, 4, 8 and 30 nodes are illustrated in (a) - (d), respectively.

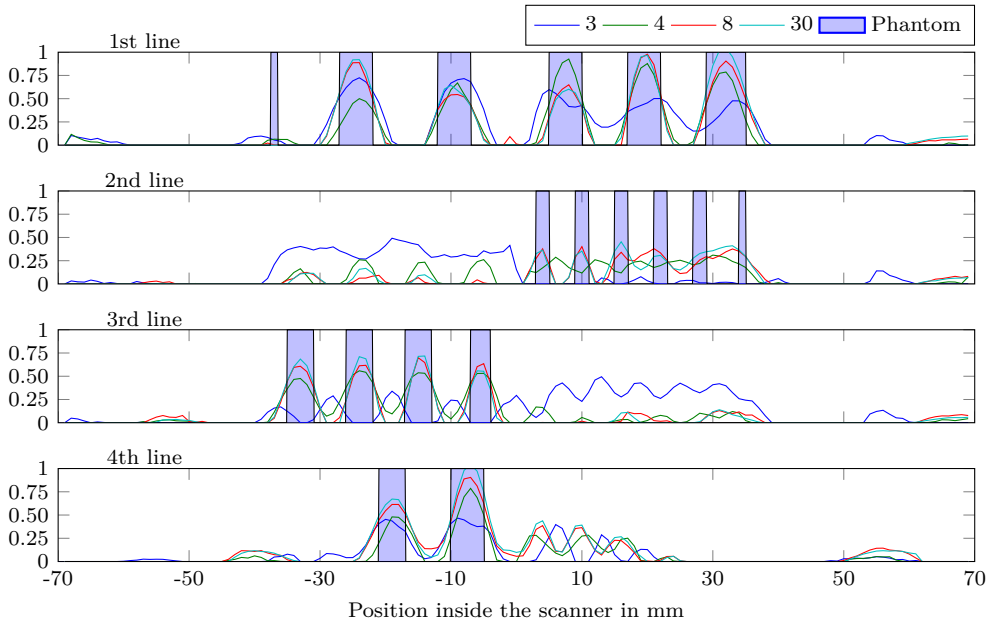

Figure 11: Line profiles (as shown in Fig. 3(a)) for the reconstructions obtained with our method using different numbers N for the approximation of the Langevin function.

(a) (b) (c)

Figure 12: Reconstruction with three different discretization schemes. (a) Secant, equidistant; (b) Tangent, equidistant; (c) Tangent, L_1-optimal.

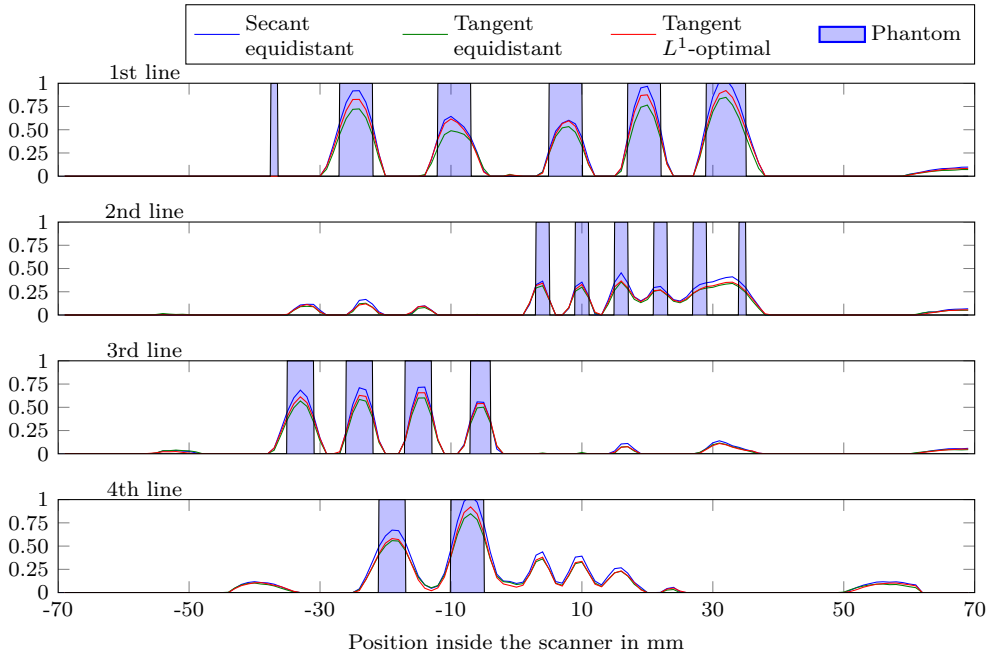

Figure 13: Line profiles (as shown in Fig. 3(a)) for the reconstructions obtained with our method using the three discretization techniques given in Fig. 12.

7. Conclusion

We introduced a new 3D modelling framework for Magnetic Particle Imaging that includes classical MPI models based on ideal 1D-FFP and FFL magnetic fields, as well as realistic magnetic field topologies. Via expansions in spherical harmonics, this framework allows to incorporate realistic magnetic fields in the imaging model such that the reconstruction process can be adapted to a given scanner topology. In this sense, our framework can be regarded as a hybrid model-based approach for MPI in

which the applied magnetic fields are measured in a preliminary calibration step and then included in the 3D model. A further advantage of our model is that no speed normalisation of the LFV is required (as preprocessing step) during the reconstruction which leads to an improved stability and avoids singularities.

Compared to an ideal FFP or FFL topology, the magnetic fields generated in real MPI scanners have distortions that lead to distorted LFVs. Our model-based approach is able to deal with these distortions and can generally be applied for magnetic fields that are parallel to their velocity field. We showed how this new 3D model can be approximated and discretized numerically in order to obtain a finite system matrix for the reconstruction of the magnetic particles.

To obtain the final magnetic particle distribution, we solved the linear system of equations (see Section 5.4) iteratively using a finite number of LSQR iterations and no further tuning. This was sufficient to evaluate the enhanced reconstruction properties of our proposed model, leaves however room for further improvements. In particular, a combined optimization of the various parameters of the model, of the discretization strategy, and the early stopping of the LSQR solver might improve the reconstruction even further. Moreover, the incorporation of more advanced regularization techniques, as for instance TV-regularization, is likely to have an additional positive effect on the reconstruction quality of our model.

Acknowledgements

The authors of this article were involved in the activities of the DFG-funded scientific network MathMPI (ER777/1-1) and thank the German Research Foundation for the support.

8. Appendix

8.1. Magnetic field topology for an ideal 3D-FFP along a Lissajous trajectory

As an important example of a magnetic field topology in MPI, we give a mathematical description of the building elements of the magnetic field $\boldsymbol{B}(\boldsymbol{r},t)$ in the original Philips design [32]. In this field topology an FFP along a 3D-Lissajous trajectory inside a cuboid domain is created. The spherical harmonic coefficients of the involved drive and selection fields are summarized in Table 3. Here, the constant g denotes the gradient strength of the selection field, d_x, d_y, d_z, and f_x, f_y, f_z the amplitudes and frequencies of the time-dependent drive field. The entire magnetic field $\boldsymbol{B}(\boldsymbol{r},t)$ to generate the 3D-FFP on the Lissajous curve is then given by

$$\begin{aligned}\boldsymbol{B}(\boldsymbol{r},t) &= \boldsymbol{B}_{\mathrm{Selection}}(\boldsymbol{r}) + \boldsymbol{B}_{\mathrm{x-drive}}(\boldsymbol{r})\ \sin 2\pi f_x t \\ &\quad + \boldsymbol{B}_{\mathrm{y-drive}}(\boldsymbol{r})\ \sin 2\pi f_y t + \boldsymbol{B}_{\mathrm{z-drive}}(\boldsymbol{r})\ \sin 2\pi f_z t \\ &= g\begin{pmatrix}-x\\-y\\2z\end{pmatrix} + \begin{pmatrix}d_x \sin 2\pi f_x t\\ d_y \sin 2\pi f_y t\\ d_z \sin 2\pi f_z t\end{pmatrix}. \end{aligned} \tag{20}$$

The vector field $\boldsymbol{B}(\boldsymbol{r},t)$ is curl- and divergence free with the potential function

$$\varphi_{\boldsymbol{B}}(\boldsymbol{r},t) = g(z^2 - \tfrac{x^2}{2} - \tfrac{y^2}{2}) + d_x x \sin(2\pi f_x t) + d_y y \sin(2\pi f_y t) + d_z z \sin(2\pi f_z t).$$

Table 3: Spherical harmonics encoding of an ideal magnetic field topology generating a 3D Lissajous FFP

Coil name	B_1	B_2	B_3	Time dependent part
Selection	$c_{11}^1 = -g$	$c_{1-1}^2 = -g$	$c_{10}^3 = 2g$	1
x-drive	$c_{00}^1 = d_x$			$\sin 2\pi f_x t$
y-drive		$c_{00}^2 = d_y$		$\sin 2\pi f_y t$
z-drive			$c_{00}^3 = d_z$	$\sin 2\pi f_z t$

The field-free point $\boldsymbol{r}_{\mathrm{FFP}}(t)$ itself is the point in $\mathbb{R}^3$ at which the magnetic field $\boldsymbol{B}(\boldsymbol{r}, t)$ vanishes, i.e., $\boldsymbol{B}(\boldsymbol{r}_{\mathrm{FFP}}(t), t) = \boldsymbol{0}$. In this example, we have

$$\boldsymbol{r}_{\mathrm{FFP}}(t) = \left(\frac{d_x}{g} \sin 2\pi f_x t, \frac{d_y}{g} \sin 2\pi f_y t, -\frac{d_z}{2g} \sin 2\pi f_z t \right).$$

In particular, the FFP moves along a Lissjous trajectory inside the cuboid domain $[-|\frac{d_x}{g}|, |\frac{d_x}{g}|] \times [-|\frac{d_y}{g}|, |\frac{d_y}{g}|] \times [-|\frac{d_z}{2g}|, |\frac{d_z}{2g}|] \subset \mathbb{R}^3$. For Lissajous FFP topologies, model-based reconstruction approaches in 3D or 2D have limitations due to the complex magnetization behavior of SPIONs. The reconstruction of the particle density for Lissajous FFP topologies is therefore usually performed by measuring the system responses in a rather time-consuming calibration procedure [10, 12, 32].

8.2. Magnetic field topology for an ideal 1D-FFP along line segments

To generate an FFP that moves along a line segment in $\mathbb{R}^3$, we can apply the field

$$\boldsymbol{B}(\boldsymbol{r}, t) = g \begin{pmatrix} -x \\ -y \\ 2z \end{pmatrix} + \begin{pmatrix} d_x \\ d_y \\ d_z \end{pmatrix} \sin 2\pi f_{\mathrm{d}} t.$$

This field can be generated in the same way as the magnetic field (20) for the 3D-FFP by using the same drive-field frequency $f_{\mathrm{d}} = f_x = f_y = f_z$ in all coordinates. The position of the FFP is then given as

$$\boldsymbol{r}_{\mathrm{FFP}}(t) = \boldsymbol{v} \sin(2\pi f_{\mathrm{d}} t), \quad \text{with} \quad \boldsymbol{v} = \left(\frac{d_x}{g}, \frac{d_y}{g}, -\frac{d_z}{2g} \right).$$

The FFP is now moving in the 1D line segment $\mathbb{L}_{\boldsymbol{v}} = \{\boldsymbol{r} = s\boldsymbol{v} \mid s \in [-1, 1]\}$. Such a 1D-FFP topology is generally used for 1D-MPI imaging, see [5, 8, 25].

8.3. The 1D-MPI imaging equation for an FFP along a line segment

As a final example of the general theory developed in this article, we show that the well-known 1D-MPI reconstruction formula for a 1D-FFP moving on an interval or a line segment in $\mathbb{R}^3$ can be deduced from Theorem 4.1. In Subsection 8.2 above, we have already seen that the magnetic field $\boldsymbol{B}(\boldsymbol{r}, t) = g(-x, -y, 2z) + (d_x, d_y, d_z) \sin 2\pi f_{\mathrm{d}} t$ leads to the FFP $\boldsymbol{r}_{\mathrm{FFP}}(t) = \boldsymbol{v} \sin(2\pi f_{\mathrm{d}} t)$ oscillating on the line segment $\mathbb{L}_{\boldsymbol{v}} = \{\boldsymbol{r} = s\boldsymbol{v} \mid s \in [-1, 1]\}$ in direction $\boldsymbol{v} = (\frac{d_x}{g}, \frac{d_y}{g}, -\frac{d_z}{2g})$. For all points $\boldsymbol{r}$ in this line segment $\mathbb{L}_{\boldsymbol{v}}$, the magnetic field $\boldsymbol{B}(\boldsymbol{r}, t)$ is parallel to its velocity field $\frac{\mathrm{d}}{\mathrm{d}t}\boldsymbol{B}(\boldsymbol{r}, t)$. Therefore,

if the support $\operatorname{supp} c = \Omega \subset \mathbb{R}^3$ of the particle concentration is located in a close volume around the line segment $\mathbb{L}_{\boldsymbol{v}}$ we can use the simplified imaging equation (9) as a model for the MPI signal generation process. Using the gradient matrix $G = \operatorname{diag}(-g, -g, 2g)$, we can write equation (9) as

$$u_\nu(t) = 2\pi\mu_0 f_{\mathrm{d}} \cos(2\pi f_{\mathrm{d}} t) \int_\Omega \left\langle \boldsymbol{\varrho}_\nu(\boldsymbol{r}), G\boldsymbol{v} \right\rangle \bar{\mathrm{m}}'(|G(\boldsymbol{r} - \boldsymbol{r}_{\mathrm{FFP}}(t))|)\, c(\boldsymbol{r})\, \mathrm{d}\boldsymbol{r}.$$

Assuming that the coil sensitivity is constant $\boldsymbol{\varrho}_\nu(\boldsymbol{r}) = \boldsymbol{\varrho}_\nu$, this equation simplifies to the 1D-MPI model

$$u_\nu(t) = 2\pi\mu_0 f_{\mathrm{d}} \cos(2\pi f_{\mathrm{d}} t) \left\langle \boldsymbol{\varrho}_\nu, G\boldsymbol{v} \right\rangle \Big(c * \bar{\mathrm{m}}'(|G \cdot|) \Big)(\boldsymbol{r}_{\mathrm{FFP}}(t)), \tag{21}$$

where $c * \bar{\mathrm{m}}'(|G \cdot|)$ denotes the convolution of the particle concentration c with the function $\bar{\mathrm{m}}'(|G \cdot|)$. If the Langevin model of magnetization is used, we can further express $\bar{\mathrm{m}}'$ in terms of the derivative (4) of the Langevin function.

Remark 4. Although the convolution defined in (21) is defined in terms of a three dimensional integral, the model in (21) is conceptually a one-dimensional model for the reconstruction of the particle concentration c along the line segment $\mathbb{L}_{\boldsymbol{v}}$. In a more idealized setting, we can also restrict the particle concentration c to the line $\{\boldsymbol{r} = s\boldsymbol{v} \mid s \in \mathbb{R}\}$ and formulate the model (21) in terms of a one dimensional convolution along this line. This 1D model was first formulated in [25]. In [5], a profound mathematical analysis of the corresponding imaging operator was conducted.

References

[1] K. Bente, M. Weber, M. Graeeser, T. F. Sattel, M. Erbe, and T. M. Buzug. Electronic field free line rotation and relaxation deconvolution in magnetic particle imaging. *IEEE Trans. Med. Imag.*, 34(2):644–651, 2014.

[2] L. Borg, J. Frikel, J. S. Jørgensen, and E. T. Quinto. Analyzing reconstruction artifacts from arbitrary incomplete x-ray ct data. *SIAM Journal on Imaging Sciences*, 11(4):2786–2814, 2018.

[3] G. Bringout. *Field Free Line Magnetic Particle Imaging: Characterisation and imaging device up-scaling*. PhD thesis, Universität zu Lübeck, 2016.

[4] G. Bringout and T. M. Buzug. A robust and compact representation for magnetic fields in magnetic particle imaging. *Biomedical Engineering*, 59:646–650, 2014.

[5] W. Erb, A. Weinmann, M. Ahlborg, C. Brandt, G. Bringout, T. M. Buzug, J. Frikel, C. Kaethner, T. Knopp, T. März, M. Möddel, M. Storath, and A. Weber. Mathematical Analysis of the 1D Model and Reconstruction Schemes for Magnetic Particle Imaging. *Inverse Problems*, 34:055012, 2018.

[6] M. Erbe. *Field Free Line Magnetic Particle Imaging*. Springer Vieweg, 2014.

[7] B. Gleich and J. Weizenecker. Tomographic imaging using the nonlinear response of magnetic particles. *Nature*, 435:1214–1217, 2005.

[8] P. Goodwill and S. Conolly. The X-space formulation of the magnetic particle imaging process: 1-D signal, resolution, bandwidth, SNR, SAR, and magnetostimulation. *IEEE Trans. Med. Imaging*, 29:1851–1859, 2010.

[9] P. Goodwill and S. Conolly. Multidimensional X-space magnetic particle imaging. *IEEE Trans. Med. Imaging*, 30:1581–1590, 2011.

[10] M. Grüttner, T. Knopp, J. Franke, M. Heidenreich, J. Rahmer, A. Halkola, C. Kaethner, J. Borgert, and T. M. Buzug. On the formulation of the image reconstruction problem in magnetic particle imaging. *Biomedical Engineering*, 58(6):583–591, 2013.

[11] J. D. Jackson. *Classical electrodynamics*. Wiley, New York, NY, 3rd ed. edition, 1999.

[12] C. Kaethner, W. Erb, M. Ahlborg, P. Szwargulski, T. Knopp, and T. M. Buzug. Non-equispaced system matrix acquisition for magnetic particle imaging based on Lissajous node points. *IEEE Trans. Med. Imag.*, 35(11):2476–2485, 2016.

[13] T. Kluth. Mathematical models for magnetic particle imaging. *Inverse Problems*, 34(8):083001, 2018.

[14] T. Kluth, B. Jin, and G. Li. On the degree of ill-posedness of multi-dimensional magnetic particle imaging. *Inverse Problems*, 34(9):095006, 2018.

[15] T. Kluth, P. Szwargulski, and T. Knopp. Towards accurate modeling of the multidimensional magnetic particle imaging physics. *New Journal of Physics*, 21(10):103032, 2019.

[16] T. Knopp, S. Biederer, T. Sattel, J. Weizenecker, B. Gleich, J. Borgert, and T. M. Buzug. Trajectory analysis for magnetic particle imaging. *Phys. Med. Biol.*, 54:385–397, 2009.

[17] T. Knopp and T. M. Buzug. *Magnetic Particle Imaging: An Introduction to Imaging Principles and Scanner Instrumentation*. Springer, 2012.

[18] T. Knopp, M. Erbe, S. Biederer, T. F. Sattel, and T. M. Buzug. Efficient generation of a magnetic field-free line. *Medical Physics*, 37:35–38, 2010.

[19] T. Knopp, M. Erbe, T. Sattel, S. Biederer, and T. M. Buzug. A Fourier slice theorem for magnetic particle imaging using a field-free line. *Inverse Problems*, 27:095004, 2011.

[20] T. Knopp, N. Gdaniec, and M. Möddel. Magnetic particle imaging: from proof of principle to preclinical applications. *Phys. Med. Biol.*, 64(14):124–178, 2017.

[21] J. J. Konkle, P. W. Goodwill, E. U. Saritas, B. Zheng, K. Lu, and S. M. Conolly. Twenty-fold acceleration of 3d projection reconstruction MPI. *Biomedical Engineering*, 58(6):565–576, 2013.

[22] T. März and A. Weinmann. Model-based reconstruction for magnetic particle imaging in 2d and 3d. *Inverse Problems and Imaging*, 10(4), 2016.

[23] C. C. Paige and M. A. Saunders. Algorithm 583: Lsqr: Sparse linear equations and least squares problems. *ACM Trans. Math. Softw.*, 8(2):195–209, 1982.

[24] N. Panagiotopoulos, R. Duschka, M. Ahlborg, G. Bringout, C. Debbeler, M. Graeser, C. Kaethner, K. Lüdtke-Buzug, H. Medimagh, J. Stelzner, T. M. Buzug, J. Barkhausen, F. M. Vogt, and J. Haegele. Magnetic particle imaging - current developments and future directions. *International Journal of Nanomedicine*, 10:3097–3114, 2015.

[25] J. Rahmer, J. Weizenecker, B. Gleich, and J. Borgert. Signal encoding in magnetic particle imaging: properties of the system function. *BMC Medical Imaging*, 9:4, 2009.

[26] E. Saritas, P. Goodwill, L. Croft, J. Konkle, K. Lu, B. Zheng, and S. Conolly. Magnetic particle imaging (MPI) for NMR and MRI researchers. *J. of Magnetic Resonance*, 229:116–126, 2013.

[27] H. Schomberg. Magnetic particle imaging: model and reconstruction. In *2010 IEEE International Symposium on Biomedical Imaging: From Nano to Macro*, pages 992–995, 2010.

[28] M. Storath, C. Brandt, M. Hofmann, T. Knopp, J. Salamon, A. Weber, and A. Weinmann. Edge preserving and noise reducing reconstruction for magnetic particle imaging. *IEEE Trans. Med. Imag.*, 36(1):74–85, 2017.

[29] A. Weber. *Behandlung von Imperfektionen bei Magnetic-Particle-Imaging mit Hilfe mathematischer Methoden*. PhD thesis, Universität zu Lübeck, 2016.

[30] J. Weizenecker. The Fokker–Planck equation for coupled Brown–Néel-rotation. *Phys. Med. Biol.*, 63(3):035004, 2018.

[31] J. Weizenecker, B. Gleich, and J. Borgert. Magnetic particle imaging using a field free line. *Journal of Physics D: Applied Physics*, 41(10):105009, 2008.

[32] J. Weizenecker, B. Gleich, J. Rahmer, H. Dahnke, and J. Borgert. Three-dimensional real-time in vivo magnetic particle imaging. *Phys. Med. Biol.*, 54(5):L1–L10, 2009.

[33] M. A. Wieczorek and A. Meschede. Shtools: Tools for working with spherical harmonics. *Geochemistry, Geophysics, Geosystems*, 19:2574–2592, 2018.